O3M SAF VALIDATION REPORT

Validated products:

Identifier	Name	Acronym
O3M-54	Near Real Time Total SO$_2$	MAG-N-SO2
O3M-55	from GOME-2A&B	MBG-N-SO2
O3M-09	Offline Total SO$_2$,	MAG-O-SO2
O3M-56	from GOME-2A&B	MBG-O-SO2
O3M-117	Reprocessed Total SO2 from GOME-2A&B	MxG-RP1-SO2

GOME-2A SO$_2$ VCD (DU) - 2007
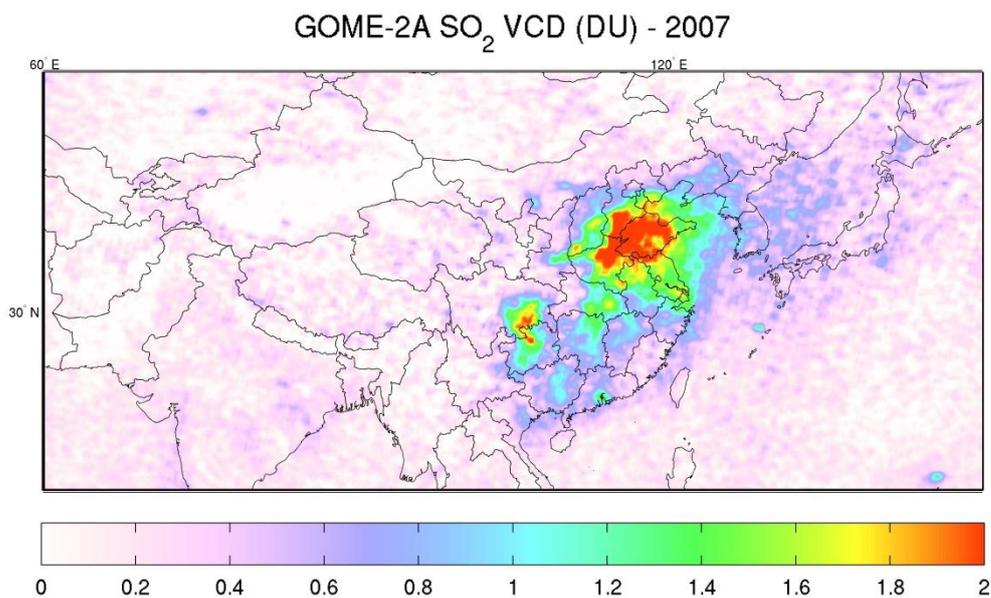
GOME-2A SO$_2$ vertical columns–2007 (China).

Authors:

Name	Institute
Nicolas Theys	Belgian Institute for Space Aeronomy
MariLiza Koukouli	Aristotle University of Thessaloniki
Gaia Pinardi	Belgian Institute for Space Aeronomy
Michel Van Roozendael	Belgian Institute for Space Aeronomy
Dimitris Balis	Aristotle University of Thessaloniki
Pascal Hedelt	German Aerospace Center
Pieter Valks	German Aerospace Center

Reporting period: GOME-2/MetOp-A Jan. 2007 – Dec. 2014
GOME-2/MetOp-B Jan. 2013 – Dec. 2014

Input data versions: GOME-2 Level 1B version 5.3.o until 17 June 2014
GOME-2 Level 1b version 6.0.0. since 17 June 2014

Data processor versions: GDP 4.8, UPAS version 1.3.9

document change record / *historique du document*

Issue	*Rev.*	*Date*	*Section*	*Description of Change*
1	0	23.09.2015	all	Creation of this document

Validation report of NRT, offline and reprocessed GOME-2 SO$_2$ column data for MetOp-A and -B

Contents

ACRONYMS AND ABBREVIATIONS

AMF	Air Mass Factor, or optical enhancement factor
BAS-NERC	British Antarctic Survey – National Environment Research Council
BIRA	Belgisch Instituut voor Ruimte-Aëronomie
CAO	Central Aerological Observatory
CNRS/LATMOS	Laboratoire Atmosphère, Milieux, Observations Spatiales du CNRS
DLR	German Aerospace Centre
DMI	Danish Meteorological Institute
DOAS	Differential Optical Absorption Spectroscopy
D-PAF	German Processing and Archiving Facility
Envisat	Environmental Satellite
ERS-2	European Remote Sensing Satellite -2
ESA	European Space Agency
EUMETSAT	European Organisation for the Exploitation of Meteorological Satellites
FMI-ARC	Finnish Meteorological Institute – Arctic Research Centre
GAW	WMO's Global Atmospheric Watch programme
GDOAS/SDOAS	GOME/SCIAMACHY WinDOAS prototype processor
GDP	GOME Data Processor
GOME	Global Ozone Monitoring Experiment
GOME-2A	Second Global Ozone Monitoring Experiment (MetOp-A)
GOME-2B	Second Global Ozone Monitoring Experiment (MetOp-B)
GVC	Ghost Vertical Column
H_2O	water vapour
IASB	Institut d'Aéronomie Spatiale de Belgique
IFE/IUP	Institut für Fernerkundung/Institut für Umweltphysik
IMF	Remote Sensing Technology Institute
INTA	Instituto Nacional de Técnica Aeroespacial
KSNU	Kyrgyzstan State National University
LOS	Line Of Sight
MIPAS	Michelson Interferometer for Passive Atmospheric Sounding
NDACC	Network for the Detection of Atmospheric Composition Change
NDSC	Network for the Detection of Stratospheric Change
NIWA	National Institute for Water and Atmospheric research
NO_2	nitrogen dioxide
O_3	ozone
O3M-SAF	Ozone and Atmospheric Chemistry Monitoring Satellite Application Facility
OCRA	Optical Cloud Recognition Algorithm
OMI	Ozone Monitoring Instrument
ROCINN	Retrieval of Cloud Information using Neural Networks
RRS	Rotational Raman Scattering
RTS	RT Solutions Inc.
SAOZ	Système d'Analyse par Observation Zénithale
SCD	Slant Column Density
SCIAMACHY	Scanning Imaging Absorption spectroMeter for Atmospheric CHartography
SNR	Signal to Noise Ratio
SO_2	Sulphur dioxide
SZA	Solar Zenith Angle

TEMIS	Tropospheric Emission Monitoring Internet Service
UPAS	Universal Processor for UV/VIS Atmospheric Spectrometers
UVVIS	ground-based DOAS ultraviolet-visible spectrometer
VCD	Vertical Column Density

DATA DISCLAIMER FOR THE GOME-2 TOTAL SO$_2$ DATA PRODUCTS

In the framework of EUMETSAT's Satellite Application Facility on Ozone and Atmospheric Chemistry Monitoring (O3M-SAF), GOME-2 SO$_2$ total column data product, as well as associated cloud parameters, are delivered in near real time and off-line. Those data products are generated at DLR from MetOp-A and MetOp-B GOME-2 measurements using the UPAS environment version 1.3.9, the level-0-to-1 v5.x and v6.0 processor and the level-1-to-2 GDP v4.8 DOAS retrieval processor. BIRA-IASB, DLR and AUTH ensure detailed quality assessment of algorithm upgrades and continuous monitoring of GOME-2 SO$_2$ data quality with a recurring geophysical validation using correlative measurements from ground-based instruments and from other satellites retrievals.

This report presents the validation of NRT, offline and reprocessed MetOp-A and MetOp-B GOME-2 SO$_2$ column data for the period 2007 to 2014, and retrieved with the GDP4.8 algorithm. The GDP v.4.8 reprocessed dataset was delivered to the validation team in late May 2015. Following the first results of the validation process which were made available to the operational team, a suite of new GDP4.8 algorithm test runs were performed for years 2008 and 2013.
The main results are summarized hereafter:

- Comparison of GDP4.7 and GDP4.8: For the slant columns, there are negligible differences between the two versions for GOME-2B while for GOME-2A the slant columns show some differences. An important feature in GOME-2A is a stronger effect of the South Atlantic Anomaly (see below). For the vertical columns, the data are found to be noisier in the new version and the GOME-2A GDP4.8 2.5km plume height product shows between 0 and 0.5-1 D.U. higher SO2 loading on a yearly basis than the GDP4.7 algorithm, whereas for GOME-2B this increase is smaller, between 0 and 0.5 D.U. at the known hot spots. Retrievals tests have shown that this was due to the use of the inverse of the Earthshine spectrum in the DOAS intensity offset correction; this issue is largely solved by using instead the inverse of the Solar spectrum. This setting is the new baseline for the GDP4.8 SO$_2$ algorithm.

- GOME-2A- GOME-2B-OMI consistency: 33 known SO$_2$ emitting locations around the world, including volcanoes, power plants, smelters, and so on, were used to compare the GOME-2A and -2B SO$_2$ to the OMI estimates. The average SO$_2$ loading of these sources was 0.41±0.31 D.U. for GOME-2A, 0.08±0.24 D.U. for GOME-2B and 0.30±0.31 D.U. for OMI. GOME-2A was found to be in better agreement with OMI than GOME-2B GDP4.8 due to the higher amount of negative mean loadings shown by the newer instrument. However, the mean correlation coefficient for these sites between GOME2 and OMI was found to be 0.42 for GOME-2A and 0.51 for GOME-2B pointing to the fact that both GOME-2A and –2B GDP 4.8 SO$_2$ column retrievals fare well with OMI/Aura considering all the limitations.

- Volcanic SO$_2$: GOME-2A and –B GDP 4.8 SO$_2$ column retrievals is clearly able to capture and track plumes after small to strong eruptions, but the newly implemented flag for volcanic SO$_2$ misses parts of aged and filamentary plumes. Quantitatively, the SO$_2$ masses estimated from GOME-2 after strong eruptions agree very well with OMI (with differences mostly within the 30% optimal accuracy), except for the rather unusual very high SO$_2$ amounts (for the first days after the start of the eruption) where GOME-2 underestimates the columns (saturation effect).

- Anthropogenic SO$_2$: the addition of a new SO$_2$ column in GDP4.8 using a typical profile for anthropogenic emissions scenario is an improvement and allows direct comparison with OMI. From

comparisons with OMI, it can be concluded that 1) several hotspots are seen by both satellite datasets and the mean values from GOME-2 and OMI are reasonably close, 2) some weak emissions are not detected by GOME-2, partly because of the better spatial resolution of OMI but also because GOME-2 data is more noisy. From the comparison (using the anthropogenic SO_2 column field) with the MAXDOAS-data, the best agreement is found for the results using clear-sky AMFs (while the results for total AMFs are always found lower). The agreement is reasonably good especially for non-winter periods and the product reaches often the target/optimal accuracy (50%/30%) and the threshold accuracy (100%) otherwise.

- Localized artifacts and product self-inconsistency: Several artifacts have been identified when viewing SO_2 maps as, for e.g., at high latitudes. Over the SAA region specifically, the GOME-2 data shows a dramatic trend over time with noisy and elevated SO_2 columns over the last years (this effect is worst in GDP4.8 than in GDP4.7). This feature is due to the treatment of the DOAS intensity offset correction. An investigation of the SO_2 SCDs over clean and polluted regions shows an anomalous dependence of the results with viewing angles for both sensors. The most likely explanation for this effect is due to differences between the slit functions used in the spectral fitting (extracted from the GOME-2 key data) and the actual ones.

A. INTRODUCTION

A.1 Scope of this document

The present document reports on the validation of NRT, offline and reprocessed GOME-2/MetOp-A and MetOp-B SO_2 column data acquired since the beginning of instrument operations. The data are produced operationally by the GOME Data Processor (GDP) operated at DLR in the framework of the EUMETSAT Satellite Application Facility on Ozone and Atmospheric Chemistry Monitoring (O3M-SAF). This report addresses the quality of individual components of the data processing, starting with DOAS fitting parameters. The report includes comparisons of GOME-2 final data products with correlative observations from independent sources, namely, total SO_2 column data produced with GDP versions 4.7, OMI and MAX-DOAS observations.

A.2 Preliminary remarks

The aim of the present document is to report on the validation of the GOME-2 SO_2 columns from MetOp-A and MetOp-B (hereafter referred as GOME-2A and GOME-2B, respectively) against various satellite data sets and ground-based data.

Reported validation studies were carried out at the Belgian Institute for Space Aeronomy (IASB-BIRA, Brussels, Belgium), at the Aristotle University of Thessaloniki (AUTH) and at DLR Remote Sensing Technology Institute (DLR-IMF, Oberpfaffenhofen, Germany) in the framework of EUMETSAT Satellite Application Facility on Ozone and Atmospheric Chemistry Monitoring (O3M-SAF).

A.3 Plan of this document

This document is divided in three main parts, addressing first of all the account of the retrieval settings applied for the SO_2 product including a detailed description of the changes brought by GDP4.8 compared to GDP4.7. Then, the GDP4.8 GOME-2A and GOME-2B Slant and Vertical column products are evaluated against the equivalent GDP4.7 products as well as OMI/Aura measurements. The anthropogenic SO_2 products are studied using known hot-spots on a global scale and are also validated against a MaxDOAS ground-based instrument located in China. The volcanic SO_2 product is also examined in detail through inter-comparisons of the different algorithm settings as well as towards OMI/Aura findings. The stability of the GOME-2A and GOME–2B SO_2 column products as a function of time is also inspected in detail.

B. DATA DESCRIPTION

B.1 SO$_2$ columns retrieval: algorithm description and changes relative to GDP4.7

B.1.1 Algorithm description

The operational retrieval of total SO$_2$ columns from the GOME-2 instrument aboard MetOp-A and –B involves a two-step procedure:

First, a DOAS retrieval is performed in the wavelength region 315-326nm, in which cross-sections of SO$_2$, O$_3$ and NO$_2$ are fitted to the UV Earth reflectance spectrum. The retrieved SO$_2$ slant column is then corrected for any instrumental bias by applying a latitude and surface-altitude dependent offset correction. The correction factors are determined in 14-days moving time window. The corrected slant columns are then corrected for the atmospheric temperature in which the SO$_2$ concentration is expected. This is a priori not known, hence the user is provided with a set of SO$_2$ results for a set of three pre-defined volcanic and one anthropogenic scenario.

Secondly, the background and temperature corrected slant columns are converted to total vertical columns by means of an Air Mass Factor (AMF). Again, for every scenario a single-wavelength AMF (at 320nm) is applied. This AMF is based on a priori profile shapes for volcanic eruption scenarios (i.e. Gaussian shaped at prescribed plume heights) and for the anthropogenic SO$_2$ column product based on aircraft measurements from Taubmann et al. (2006).

B.1.2 Changes relative to GDP v4.7

In a previous validation report (Theys et al., 2013), SO$_2$ columns retrieved from GOME-2/MetOp-A &-B using the operational GDP4.6 processor were evaluated for the years 2007 to 2013. Since 2013 GOME-2/MetOp-B data is provided on an operational basis.

In order to provide an improved dataset and to fulfill user demands, an updated operational processor version 4.8 was developed. This updated version incorporates the following points:

- Harmonization of retrieval settings between both GOME-2 sensors

    In GDP4.7 a different treatment of instrumental straylight was used for both instruments: For GOME-2A an inversed solar irradiance spectrum was fitted in the DOAS retrieval, whereas for GOME-2B an inversed Earthshine spectrum was used. The usage of an inversed Earthshine spectrum follows directly from the linearization of Beer's Law when an offset term is added. Also the polynomial degree to correct for broadband absorption features was different (3rd order for GOME-2A and 5th order for GOME-2B). In order to use harmonized settings for both sensors it was decided to use an inversed Earthshine spectrum for the straylight correction and a 5th order polynomial for the GDP4.8 dataset that is validated in this report. Note that at a later stage after a first draft version of this verification report, it was found that using an inversed Earthshine spectrum results in an increased noise level and long-term trends. The final GDP4.8 dataset to be released will thus incorporate an inversed solar irradiance spectrum for both instead.

- Improved retrieval settings

    The SO2 cross-section used for the retrieval are based on SCIAMACHY flight model measurements. In order to apply them to GOME-2 data it is required to deconvolve the cross-section with

SCIAMACHY slit function data and convolve it with the appropriate GOME-2 slit function. An updated deconvolution process was implemented for GDP v4.8 improving the quality of the SO_2 cross-section data and thus the SO_2 retrieval

- New anthropogenic SO_2 scenario

In GDP4.7 only a set of three total SO_2 vertical columns have been provided for three volcanic eruption scenarios (i.e. SO_2 plumes at 2.5, 6, and 15km). It is however of increasing interest of the user community to also have SO_2 retrievals for anthropogenic pollution scenarios, for which the 2.5 km plume height scenario is clearly not appropriate. Thus, for GDP 4.8 an anthropogenic SO_2 profile is used for the generation of AMFs. This profile is based on aircraft measurements (Taubmann et al. 2006)

- Flagging of volcanic SO_2 plumes

A new volcanic activity detection algorithm has been implemented in the operational GDP v4.8 retrieval. This algorithm is based on algorithm used by the SACS project (Support to Aviation Control Service) and described in Brenot et al. (2014). The original SACS algorithm was adjusted to identify the entire volcanic SO_2 plume using different threshold values for the vertical SO_2 column depending on the proximity to known volcanoes or polluted areas (anthropogenic or the SAA). In the final product a new flag was added that provides the user with the information whether a pixel shows increased SO_2 values due to volcanic activity. In order to reduce false-positive detections over polluted areas the flag can take different values. However it should be noted that the detection algorithm is very conservative and so far no false-positive detection have been found, even in polluted areas.

- Cloud algorithm changes

Within GDP4.7, geometric cloud fractions determined by OCRA/ROCINN were employed. It is however found that it is better to use Intensity weighted Cloud Fractions (IWCF) that take into account the wavelength dependency of the cloud fraction. There is no dedicated algorithm to calculate this for the SO_2 fit window (315-326nm) and hence, in GDP4.8, the IWCF explicitly calculated from the O_3 fit window (325-335nm) is used. This wavelength window is of course not the same as for the 315-326nm window but is a much better estimate as using the geometric cloud fraction enforced so far.

Table I. DOAS settings used for the GOME-2 SO_2 retrieval GDP4.8.

Fitting interval	315 – 326 nm
Sun reference	Sun irradiance for GOME-2 L1 product
Wavelength calibration	Wavelength calibration of sun reference optimized by NLLS adjustment on convolved Chance and Spurr solar lines atlas
Absorption cross-sections	
- SO_2	Updated reconvolved SCIA Flight Model [Bogumil et al., 2003], 203K (15 km)
- NO_2	GOME-2 Flight Model/CATGAS [Gür et al., 2005], 241 K
- O_3	Brion et al. [1998], 218 K and 243 K, reconvolved at GOME-2 resolution Two pseudo-cross-sections accounting for interference between SO_2 and O_3
- Ring effect	2 Ring eigenvectors generated using SCIATRAN

- Instrumental straylight	Inversed earthshine spectrum from L1 data (original verification dataset)
	Inversed solar spectrum from L1 data (revised final verification dataset)
Polynomial	5th order (6 parameters)
SCD background correction	Latitude and surface-altitude dependent offset, determined from a 14day moving average

B.2 Validation datasets

The SO_2 columns in the atmosphere may vary greatly from about 1DU level for anthropogenic SO_2 and low level volcanic degassing to 10-1000DU for medium to extreme volcanic explosive eruptions. This wide range of possible values/scenarios makes any attempt to validate the GOME-2 total SO_2 column product a difficult task:

- Anthropogenic/boundary layer SO_2: the measurement of SO_2 is a challenge because of the low column amount (especially for GOME-2 at moderate spatial resolution) and reduced measurement sensitivity close to the surface and the SO_2 signal is generally overwhelmed by the competing O_3 absorption. The column accuracy is directly affected by the quality of the background correction applied. In this work, we will use SO_2 column (and profile) retrievals from a ground-based MAX-DOAS instrument at Xianghe, China (Wang et al., 2014) to validate the GOME-2 SO_2 products. No attempts will be made to use the Brewer Network as the data quality is deemed insufficient for validation of anthropogenic SO_2.

- Volcanic SO_2: the measurement is facilitated by large SO_2 columns generally at high altitudes (free-troposphere to lower stratosphere). However, for large SO_2 columns (typically >50 DU) the SO_2 absorption tends to saturate leading to a general underestimation of the SO_2 columns, affecting directly the product accuracy. For most volcanoes, there is generally no ground-based equipment to measure SO_2 during an appreciable eruption and even if it is the case, the data are generally very difficult to use for validation. In practice, dedicated aircraft campaign flights can also measure volcanic SO_2 clouds, but rely on the occurrence of volcanic events and there is only a handful of datasets available. In the present study, the approach that has been adopted is to verify/validate the GOME-2 SO_2 column product through cross-comparisons with SO_2 column products from OMI.

Before showing any results, it is good to recall the user requirements for the GOME-2 SO_2 products in terms of accuracy as these numbers will guide us in the present report: Threshold accuracy: 100%; Target accuracy: 50% (for solar zenith angles lower than 70°); Optimal accuracy: 30%. These numbers are taken from the O3MSAF Service Specification Document, available at
http://o3msaf.fmi.fi/docs/O3M_SAF_Service_Specification.pdf.

C. EVALUATION OF THE SO2 COLUMN DATA PRODUCT

Before showing results, it is important to remind the evolution of the data quality as a function of time. Figure 1 illustrates the fitting residuals and slant column errors (averaged over the equatorial pacific) as a function of time, both for GOME-2 onboard MetOp-A and MetOp-B (hereafter referred as GOME-2A and GOME-2B, respectively). From Figure 1, one can see the GOME-2A suffers for many years of a strong instrumental degradation affecting the quality of the SO2 column product (e.g., the data scatter has more than doubled since the beginning of operations) but after the 2009 throughput test the residual are reasonably stable over time. The GOME-2B data starting from Dec. 2012 seems to be of similar quality than GOME-2A in early 2007 (beginning of operations) but one can also see a quite strong increase of the residuals and data scatter as a function of time.
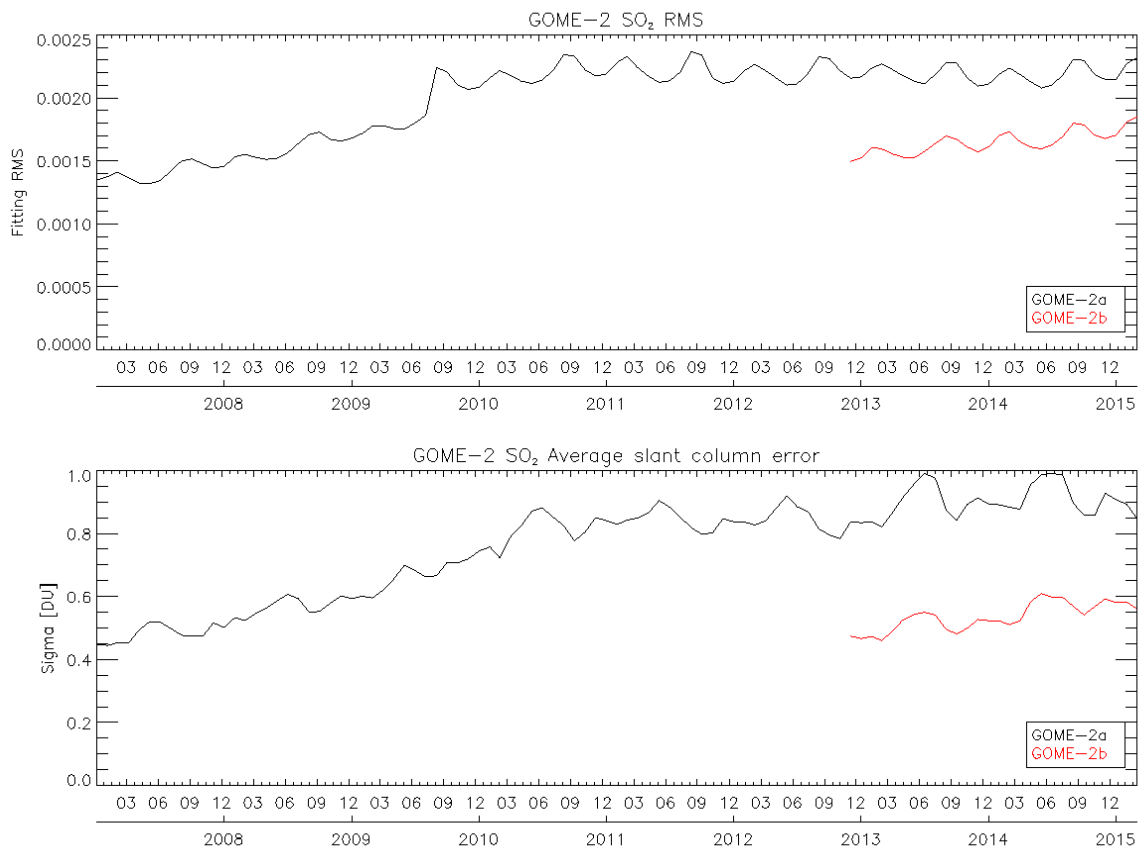

Figure 1. Average DOAS fitting residuals (upper panel) and slant column error (lower panel) in the equatorial Pacific (Lat: 20N-20S, Lon: 160W-160E) as a function of time for GOME-2A (black) and GOME-2B (red).

In the following, we will first evaluate the SO_2 at the global scale (section D1) by comparing GDP4.7 and GDP 4.8 but also assess the consistency of GDP4.8 GOME-2A, GOME-2B and OMI results. In section D2, we will focus more in details on several comparison cases for volcanic and anthropogenic SO_2 scenarios.

C.1 Verification of SO$_2$ vertical columns at the global scale

C.1.1 Data sets and methodology

The GOME2/MetopA and GOME2/MetopB GDP4.7 total SO$_2$ column measurements contain three different column products: one assuming the SO$_2$ load is located near the planetary boundary layer at 2.5km altitude, one assuming the SO$_2$ is located in the free troposphere at 6km altitude and one assuming the SO$_2$ has volcanic eruptive provenance and has crossed the tropopause and is located at 15km altitude. For the following comparisons, the lowermost column [reported at 2.5km] will be utilized.

The GOME2/MetopA and GOME2/MetopB GDP4.8 total SO$_2$ column measurements contain, additionally to the columns described above, a column at 1km, of pure anthropogenic provenance. For the GDP4.8 datasets hence both the data associated with this column, as well as the traditional 2.5km column as well as this new column, will be examined in the following.

The GOME2/MetopA and GOME2/MetopB GDP4.7 & GDP4.8 SO$_2$ columns have been filtered using the following choices: data are accepted for the analysis if the associated intensity weighted cloud fraction is less than 20%, the solar zenith angle less than 60° and the quality flag as well as the SO$_2$ associated quality flag equal zero [denoting completely trouble-free data points]. Furthermore, only forward pixels from the descending node observations were allowed for these comparisons. The updated cloud algorithm retrieval associated with GDP4.8 is also expected to result in altered VCDs, due to the new associated AMF calculations.

The OMI/Aura NASA Sulphur Dioxide Level 2G Global Binned (0.125 deg Lat/Lon grids) Data Product-OMSO2G was downloaded from the GODDARD Earth Sciences Data and Information Services Center[1]. The Planetary Boundary Layer (PBL) SO$_2$ column (ColumnAmountSO2_PBL), corresponding to a Centre of Mass Altitude, CMA, of 0.9 km, was examined with the same restrictions applied above. The OMI columns will be used as a backdrop onto which the differences between GDP4.7 and GPD4.8 can be assessed and possible differences between GOME-2A and GOME-2B rooted out.

All datasets were then averaged onto a 1x1° grid on a global scale and monthly basis and the mean SO$_2$ load, associated standard deviation of the mean, average reported error value as well as the standard deviation of the error value was saved in a monthly mean data file. This gridding was also performed using an area average technique whereupon each monthly 1x1° grid was not only allocated the measurements it represented by also a weight of the eight surrounding cells, hence introducing a spatial "smoothing" which cleared-up some of the noise associated with these measurements. From the monthly mean data, seasonal and yearly mean products were created for viewing and comparison purposes. Hence, two products will be shown in the following, the simple mean and the area weighted mean.

In order to perform quantitative comparisons between the datasets, apart from the monthly, seasonal and yearly products, a sample of selected locations on a global scale was chosen for detailed study and shown in Table II. Those sites represent well-known and well-documented, as well as important, SO$_2$ sources of both natural and anthropogenic origin. For these locations, the datasets were averaged on a finer grid of 0.25x025° grid in that case around 2.5° from the location center. Scatter plots and statistics are hence presented for those sites in order to assure a high enough SO$_2$ signal from the satellite observations.

---

[1] http://disc.sci.gsfc.nasa.gov/Aura/data-holdings/OMI/omso2g_v003.shtml

Year 2008 was chosen as representative of the beginning of the GOME2/MetopA mission and year 2013 for GOME2/MetopB.

Table II. List of locations studied as major SO_2 sources on a global scale.

	LATITUDE	LONGITUDE	TYPE	NAME	LOCATION
1	-37.85	-71.16	Volcano	Copahue	Copahue
2	-26.57	29.17	Power_Plants	South_Africa	South_Africa
3	-17.63	-71.34	Smelter and Volcano	Ilo, Ubinas	Peru
4	-16.25	168.12	Volcano	Ambrym	Vanuatu
5	-8.27	123.51	Volcano	Lewotolo	Indonesia
6	-7.94	112.95	Volcano	East Java	Indonesia
7	-6.09	155.23	Volcano	Bagana	Papua New Guinea
8	-4.12	152.2	Volcano	Turvurvur/Rabaul	Papua New Guinea
9	-4.08	145.04	Volcano	Manam	Papua New Guinea
10	-1.41	29.2	Volcano	Nyiragongo	Democratic Republic of Congo
11	1.68	127.88	Volcano	Dukono	Indonesia
12	13.26	123.69	Volcano	Mayon	Philippines
13	16.35	145.67	Volcano	Anatahan	Northern Mariana Islands
14	16.72	-62.18	Volcano	Soufrière Hills	Montserrat (UK)
15	19.08	-104.28	Power Plant	Manzanillo	Mexico
16	19.4	-92.24	Oil industry	Oil fields in Gulf of Mexico	Mexico
17	19.48	-155.61	Volcano	Kilauea, Hawaii	U.S.
18	20.05	-99.28	Industrial and Volcano	Tula, Popocatepetl	Mexico
19	20.63	39.56	Oil industry	Shoaiba	Saudi Arabia
20	23.12	113.25	Multiple sources	Guangdong	China
21	29.22	50.32	Oil industry	Khark Island	Iran
22	29.98	55.86	Smelter	Sarcheshmeh	Iran
23	34.08	139.53	Volcano	Miyake-jima	Japan
24	37.12	22.11	Power_Plants	Balkans	Balkans

25	37.73	15	Volcano	Mt. Etna	Italy
26	39.44	106.72	Multiple sources	Shizuishan	China
27	39.9	116.38	Multiple sources	Eastern_China	Eastern_China
28	42.15	25.91	Power Plants	Marica	Bulgaria
29	44.67	23.41	Power Plants	Rovinary, Turceni, Isalnita	Romania
30	46.83	74.94	Smelter	Balqash	Kazakhstan
31	69.36	88.13	Smelter	Norilsk	Russia

C.1.2 Comparisons between total SO$_2$ columns by the GDP4.7 and GDP4.8 algorithms for GOME-2 MetOp-A and MetOp-B

In Figure 2 the global SO$_2$ load at 2.5km seen by GOME-2A is given for the current GDP4.7 (left) and the new GDP4.8 (right) algorithms. Year 2008 was chosen as it was the beginning for the GOME-2A mission and hence the least possible instrumental degradation is present to affect our comparisons. Even though the general features appear similar, a number of issues may already be identified such as the South Atlantic Anomaly (SSA) producing high SO$_2$ values in the new version of the data. Some of the higher values in the high latitudes of the Northern Hemisphere, especially in North America/Canada but also in Siberia, are attributable to the Kasatochi Volcano, an active stratovolcano, in the Aleutian Islands of Southwestern Alaska.
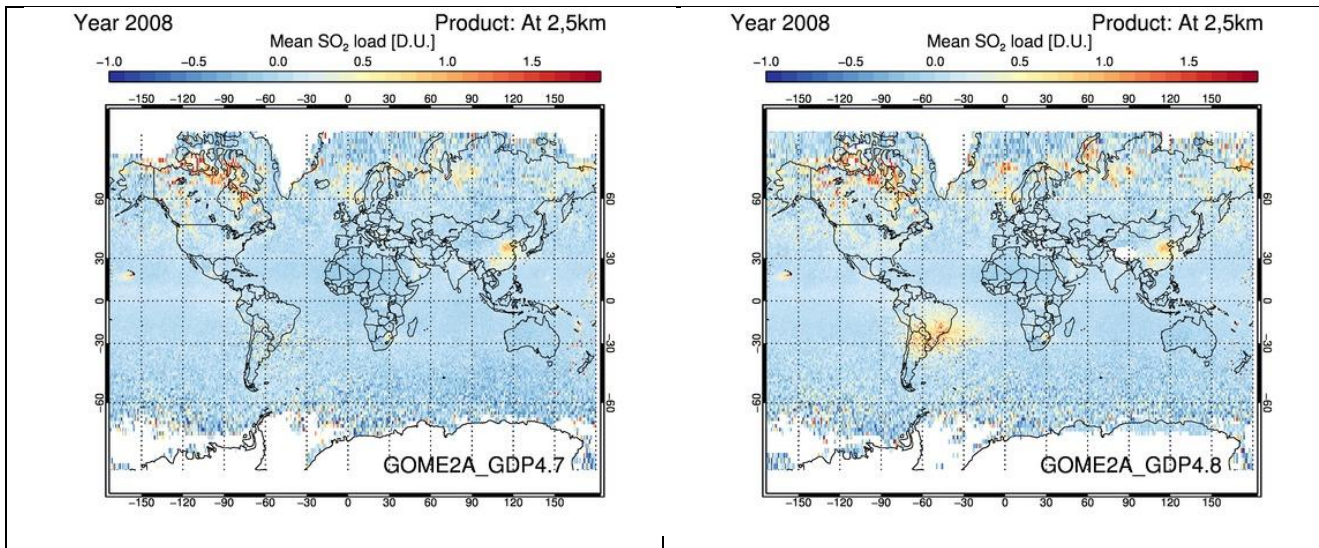

Figure 2: The global SO$_2$ load at 2.5km as seen by GOME-2A GDP4.7 (left) and GDP 4.8 (right) is shown for year 2008.

In Figure 3 the global mean SO$_2$ load at 2.5km seen by GOME-2B is given for the current GDP4.7 (left) and the new GDP4.8 (right) algorithms for year 2013, the beginning of the MetopB mission. It is obvious that the data is far less noisy, with the abnormally high values in the Northern high latitudes disappearing and known hot spots appearing clearly such as the Nyiragongo and Nyiamuragira Volcanoes, in the Democratic Republic of Congo, in Africa, volcanic activity from Popocatepetl as well as industrial activity in Mexico, in addition to the industrial regions south of Beijing in China. Some issues remain for the SAA region while it

appears as though the GOME-2B GDP4.8 algorithm is producing lower SO_2 loading than the GDP4.7 algorithm, to be discussed further below.
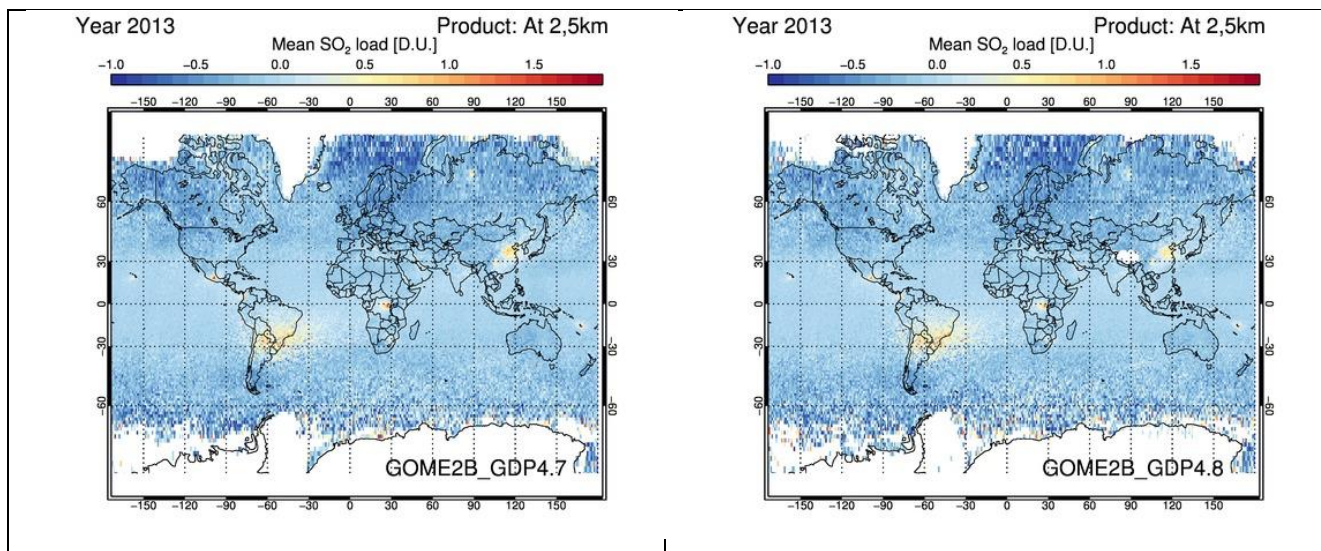
**Figure 3.** The global SO_2 load at 2.5km as seen by GOME-2B GDP4.7 (left) and GDP 4.8 (right) is shown for year 2013.
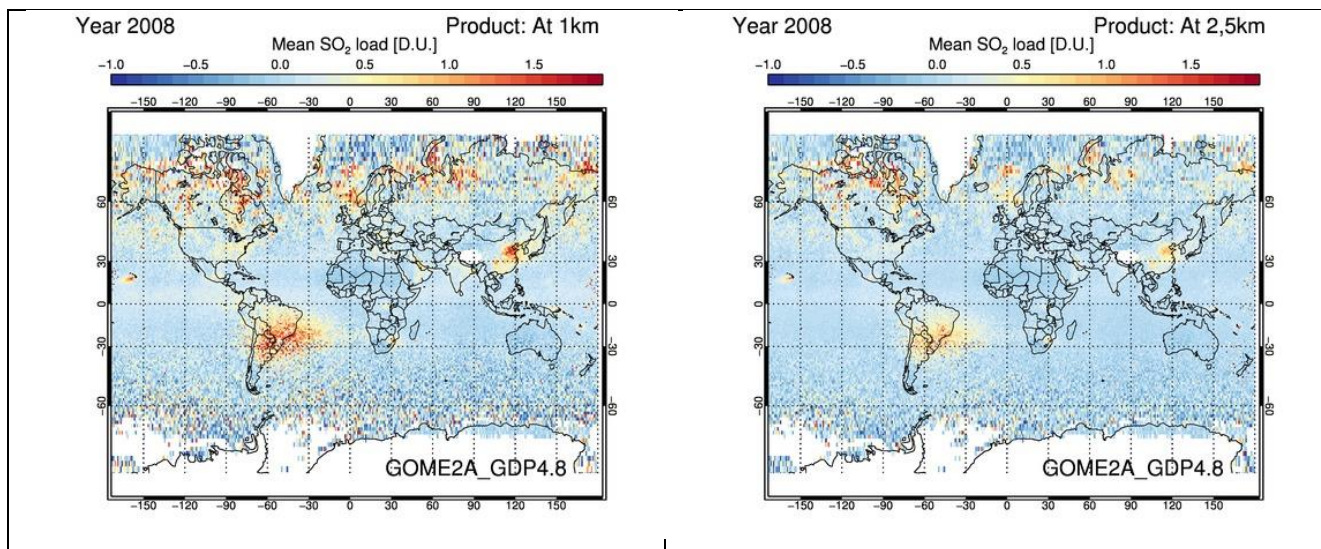

Figure 4. The global SO_2 load at 1km (left) and 2.5km (right) as seen by GOME-2A GDP4.8 is shown for year 2008.

In Figure 4 a first visual comparison is shown for the new 1km anthropogenic product (left) provided by the GDP4.8 algorithm against the traditional 2.5km product (right) for year 2008. Undoubtedly, the 1km product is, as expected from the lower AMFs, noisier on a global scale and seems to provide higher SO_2 values at the known hot-spots, with the Kīlauea eruptions in Hawaii appearing stronger, as well as the hotspots in China. As discussed above, the similar picture for GOME-2B GDP4.8 (Figure 5) is less noisy, even though the SSA area is still noisier due to the lower AMFs calculated and the signal retrieved for the 1km product is indeed higher.
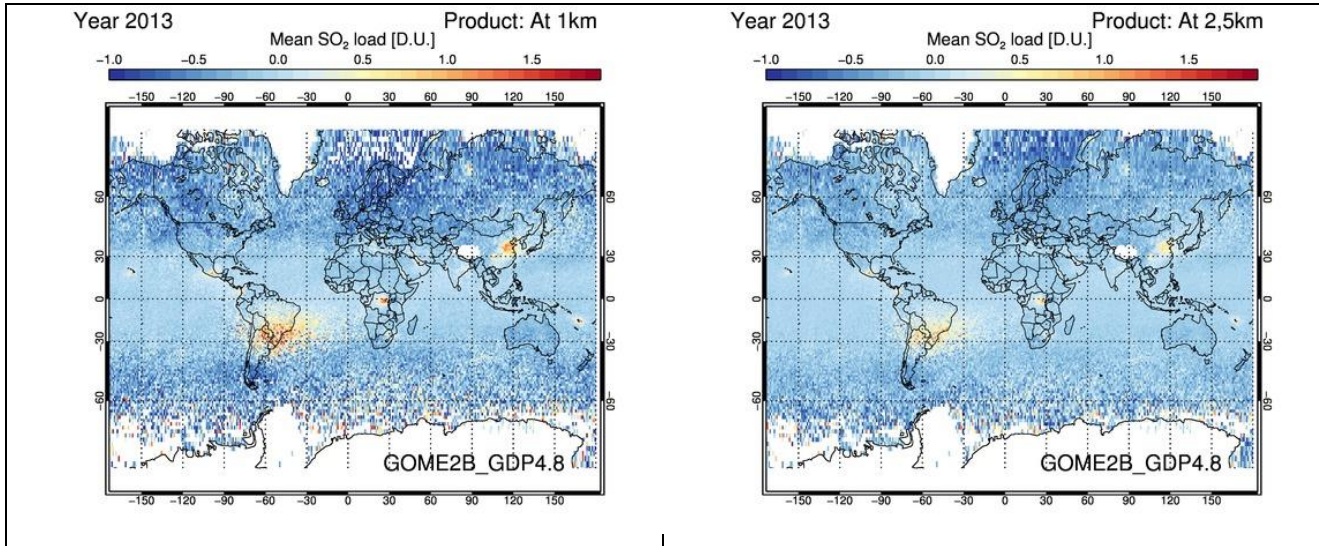
Figure 5. The global SO$_2$ load at 1km (left) and 2.5km (right) as seen by GOME-2B GDP4.8 is shown for year 2013.

A simple example of the actual differences between the new algorithm and the current one is given in Figure 6 for China. In the first row, the differences between GOME-2A GDP4.8 and GDP4.7 for year 2008, in the middle row, the differences between GOME-2A GDP4.8 and GDP4.7 for year 2013 and in the bottom row, the differences between GOME-2B GDP4.8 and GDP4.7 for year 2013.

The absolute differences are shown since most pixels in this domain are related to near-zero values which made a very noisy percentage difference plot. In the left column, the differences of the row plots shown in Figure 6 reveal the higher SO$_2$ value reported by GOME-2A GPD4.8 for the hotspot region in China of almost 50% for the entire polluted region and of close to 10-20% and only for some central spots for GOME-2B. For GOME-2A for the year 2008 [top row] no variations are seen in the absolute differences of the hotspots. Year 2013 [middle and bottom rows] is obviously noisier due to the instrumental degradation effects. However, the actual differences in the SO$_2$ sources remain of the same order of magnitude irrespective of the year shown.

In the right column of Figure 6 we give the differences for the area weighted mean SO$_2$ load. Even though for such a coarse grid of 1x1° this dataset can only be used for pictorial reasons, the high latitude issues identified in previous Figures are revealed here, Northwards of 55°N, where the SO$_2$ field is no longer smooth but strong pixelation appears.

The Himalayan plateau appears white [i.e. no data] since no GDP4.8 retrievals passed the restriction selection enumerated in Section C.1.1.
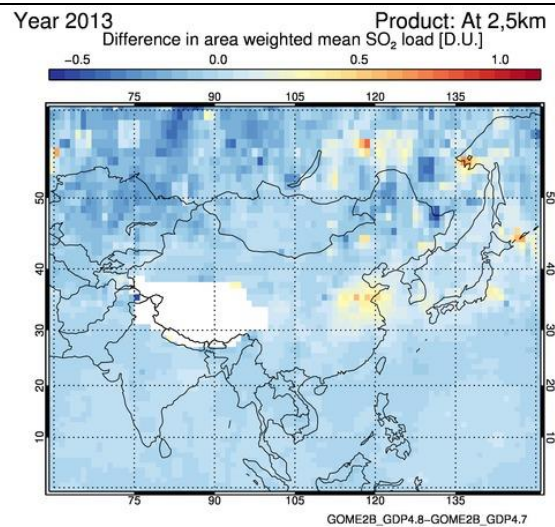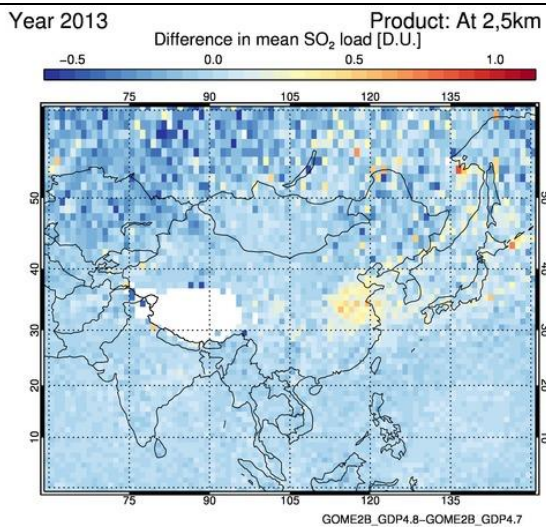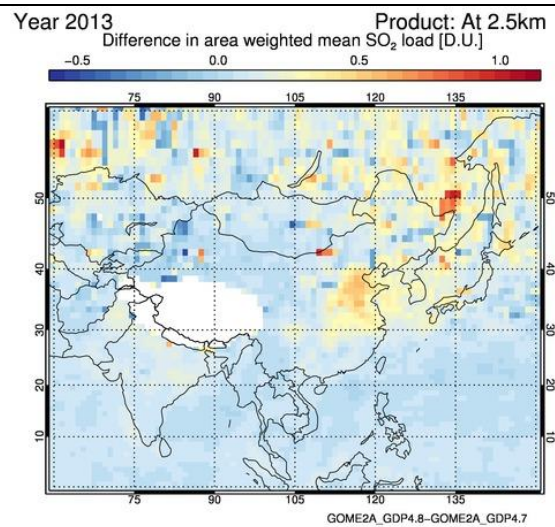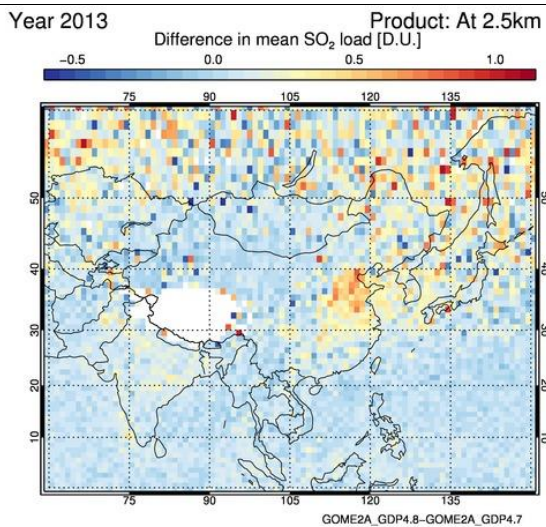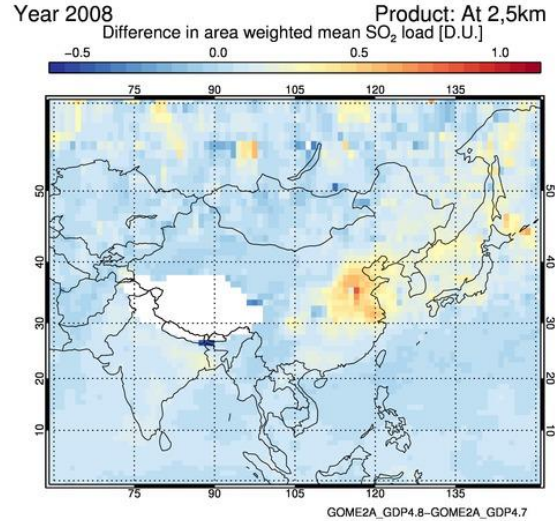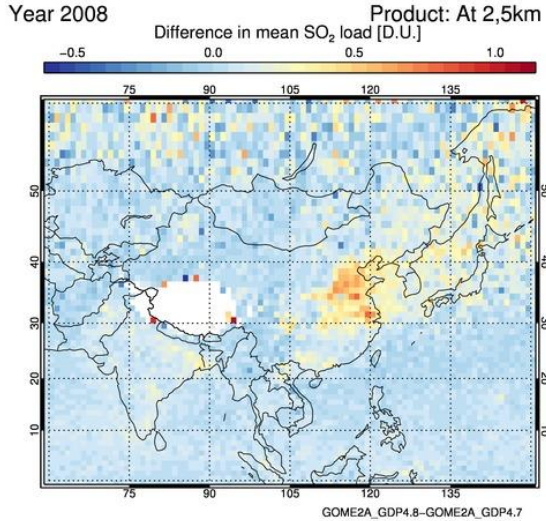
Figure 6. Left column. Absolute differences between GOME-2A GDP4.8 and GDP4.7 for 2008 [top]; same for 2013 [middle] and between GOME-2B GDP4.8 and GDP4.7 for 2013 [bottom]. **Right column.** Same as the left column, but for the area weighted mean SO$_2$ load.

In the next section the aim is to show that the two instruments see the same atmospheric state, analyzed with either the new GDP4.8 algorithm or with the original GDP4.7 one. Year 2013 will be used as a reference point. The new algorithm is expected to homogenize the SO$_2$ loadings seen by the two instruments and to have improved issues already identified in the previous validation effort such as the general tendency of GOME-2B to produce lower columns than GOME-2A by about 5-10% depending on the region examined. From Figure 7, where the comparison is shown for the Asia region for year 2013 for both algorithms and instruments we can already see the differences between the two instruments already identified in the previous validation effort (top row). These differences do not appear to be smoothed out with the new algorithm (bottom row). GOME2-A for year 2013 is generally noisier. For GOME-2B, it can be seen that the higher values over the Eastern China are a bit lower in GDP4.8 and 4.7 (possibly because of the different cloud algorithm leading to a slightly different cloud masking). The noise on the GOME2 (A and B) VCDs seems to be higher as well for the new algorithm.
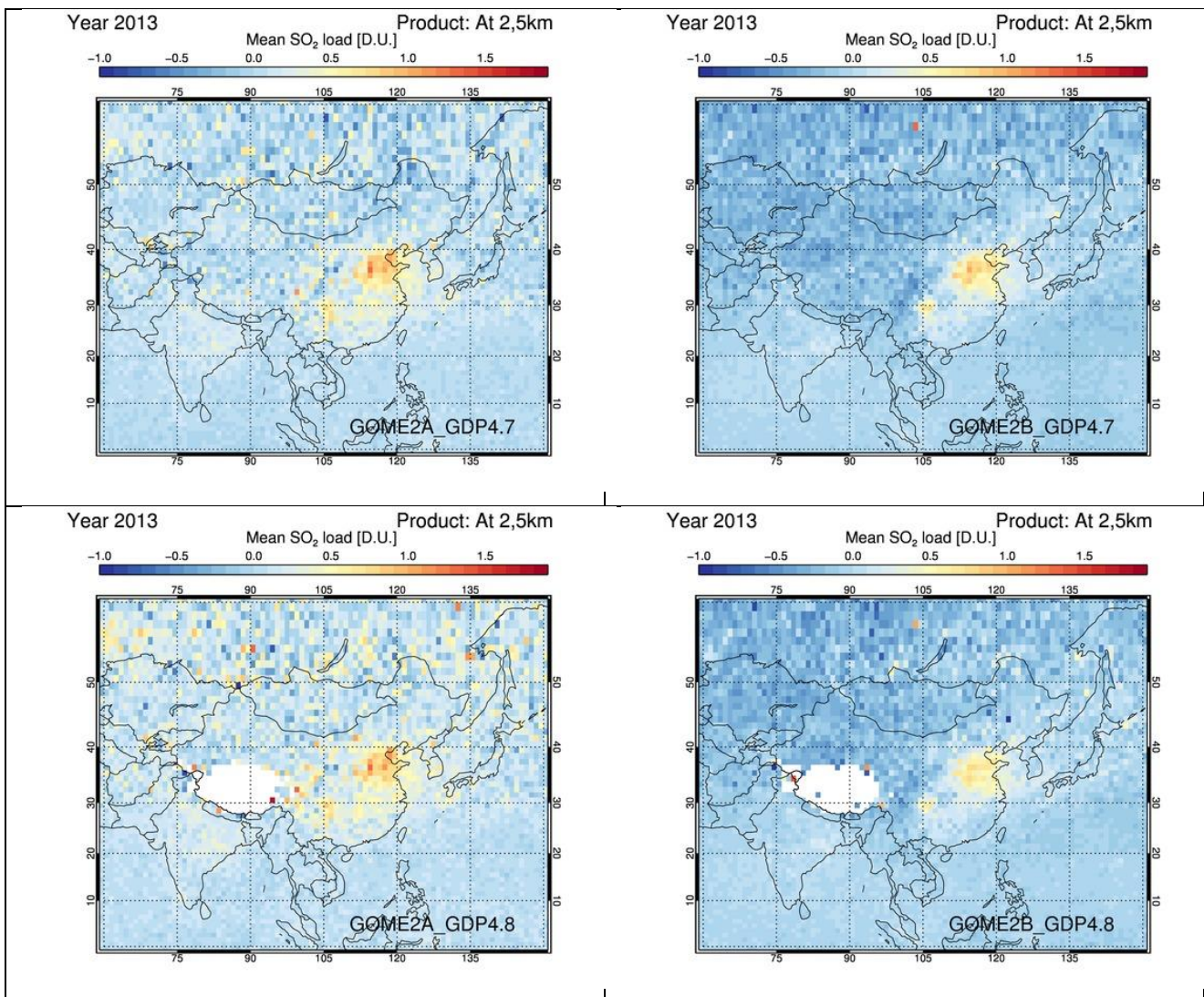
Figure 7: Comparison between GOME-2A and GOME-2B GDP4.7 (upper) and GDP4.8 (lower) for year 2013 zooming into Asia. GOME-2A is on the left and GOME-2B on the right column.
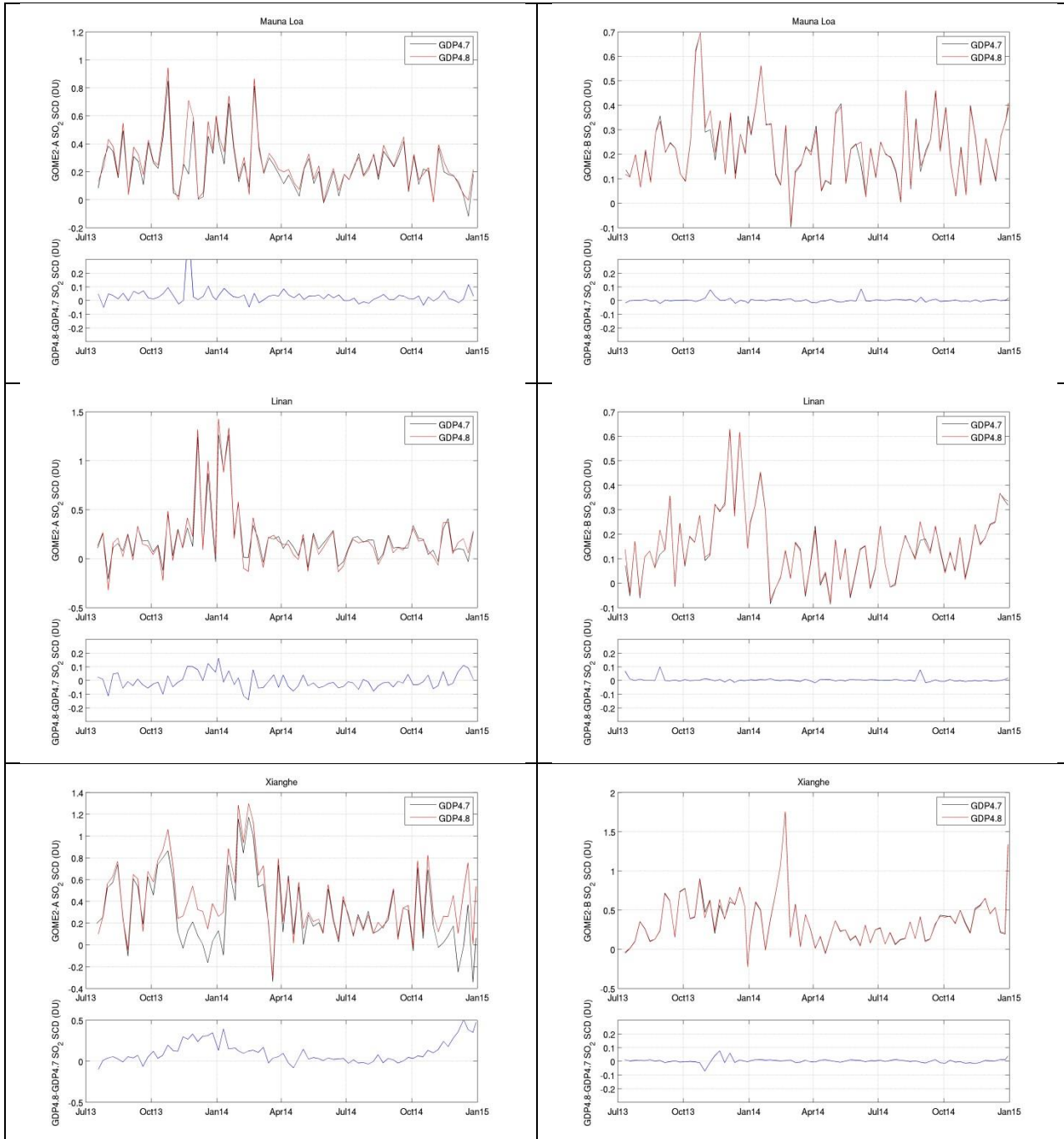

Figure 8. Time-series of weekly averaged SO2 background corrected slant columns over Mauna Loa (19.53°N,155.58°W), Linan (30.3°N, 119.73°E) and Xianghe (39.98°N, 116.37°E) for GOME-2A (left plots) and GOME-2B (right plots) comparing GDP versions 4.7 (black line) and 4.8 (red line) for the period July 2013-December 2014. The blue curves show the differences between the SO2 SCDs of versions 4.8 relative to 4.7. The pixels in a circle of 150 km radius around the stations are considered for SZA less than 70°.

Figure 8 shows examples of comparisons between SO_2 SCDs (GDP4.7 vs GDP4.8) for selected locations (Mauna Loa in Hawai in the top row, Linan and Xianghe in China in the middle and bottom rows) both for GOME-2A and –B. Generally, the GOME-2B results for the different versions are very close and the differences are always lower than 0.1 DU. This means that the differences seen in the VCDs in Figure 7 are coming from the AMFs (most likely from the update in the cloud products).

In contrast, the differences between GOME-2A GDP4.8 and 4.7 SO_2 SCDs are much larger than in the case of GOME-2B and the reason for the discrepancy for GOME-2A only is due to the fact that the upgrade from GDP4.7 to GDP4.8 for that instrument necessitated a lot more changes as seen in Section B.1.2.

In order to understand the differences between GDP4.7 and GDP4.8 SO_2 products better, several iterative discussions with the operational algorithm team at DLR have taken place. Note that most of this report is based on the original GDP v4.8 dataset delivered to the validation teams in late May 2015. Some of the problems of the new dataset identified in this report have already been taken into account in a suite of new GDP4.8 algorithm test runs performed by the operational team for years 2008 and 2013.

For GDP v.4.8 the initial idea was to harmonize the retrieval settings between GOME-2A and GOME-2B and thus using an Inversed Earthshine spectrum was selected. One important issue identified in this report is a generally higher noise level in the GDP v4.8 data, which is especially visible in the SAA region. This effect is mainly visible for the GOME-2A data and, to a lesser extent, for GOME-2B data. The reason for this was a different treatment of intensity offset correction in the DOAS retrievals for GOME-2A and GOME-2B in GDP v4.7: In GDP v4.7, for GOME-2A data an Inversed solar irradiance spectrum was fitted, whereas for GOME-2B an Inversed Earthshine spectrum was used.

After this problem was identified by the validation team, a drift analysis however revealed that using an Inversed Earthshine spectrum leads not only to much higher noise levels in the SO_2 retrieval but also causes a trend in the SO_2 dataset over regions with no known and major SO_2 sources (see red line in Figure 9). This is probably related to the degradation of the instrument which affects the Earthshine data used for the offset correction.

This higher noise level is unfortunately not visible in the daily data or on short timeframes. This is the reason why it was not identified as a problem for the GOME-2B GDP v4.7 retrieval in the last validation report.

In the new GDP v4.8 retrieval settings [see blue lines in Figure 9] both instruments now use an Inversed solar irradiance spectrum. With this, the noise levels are much reduced, especially in the SAA region. Also no drifts are visible in SO_2-free regions.
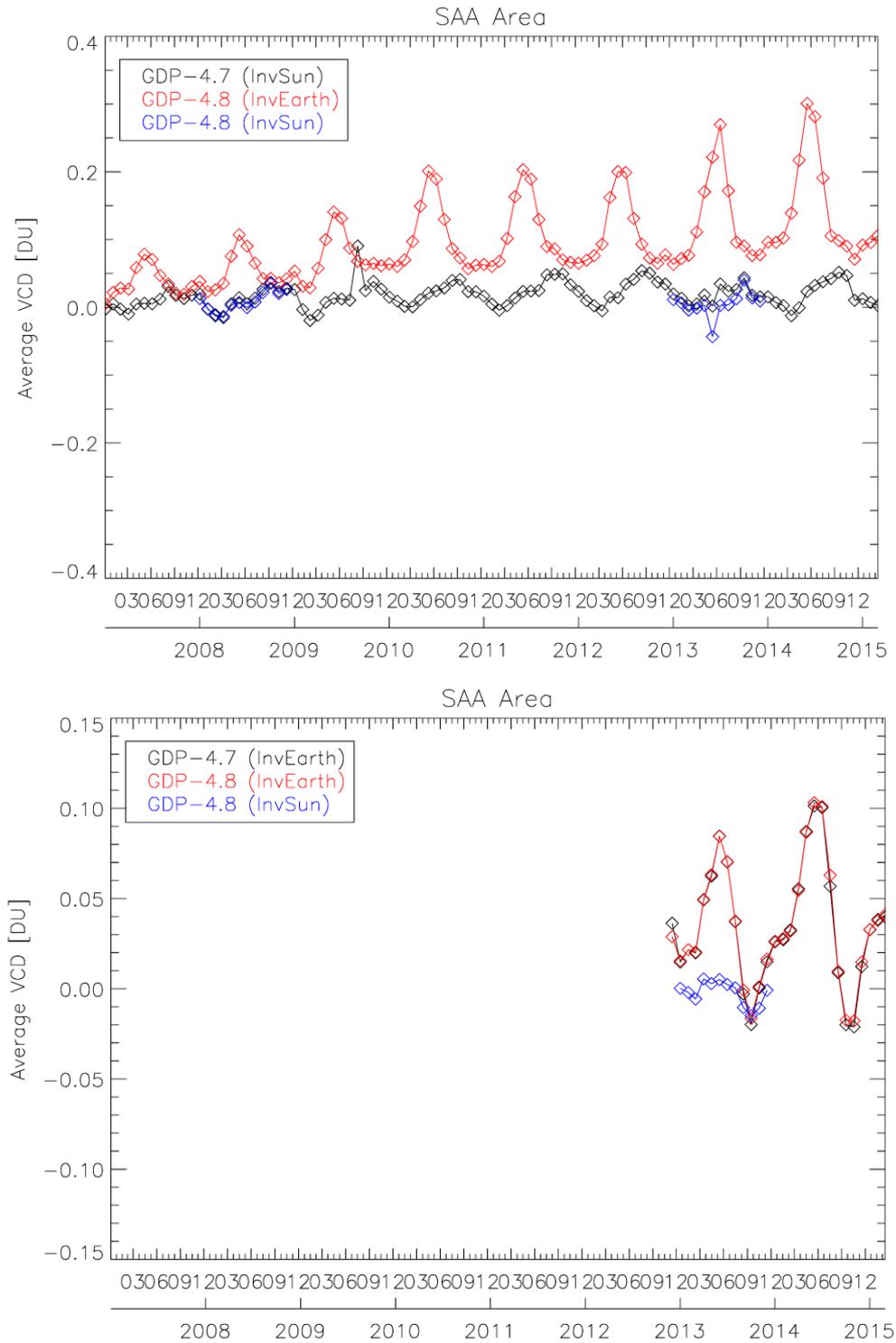
Figure 9: Monthly averaged SO_2 time series for GOME-2A (top) and GOME-2B (bottom) for the SAA region between -60°S and -10°S and -100°W and 0. Clearly visible is an increasing SO_2 trend for the GDP v.4.8 dataset used in this validation report (red). After identification of the problem, a corrected dataset has been generated for some selected years (blue).

GOME-2/MetOp-A (GDP4.7)
2013

Average SO₂ column density [DU]

Credit: DLR

GOME-2/MetOp-A (GDP-4.8)
2013

Average SO₂ column density [DU]

Credit: DLR
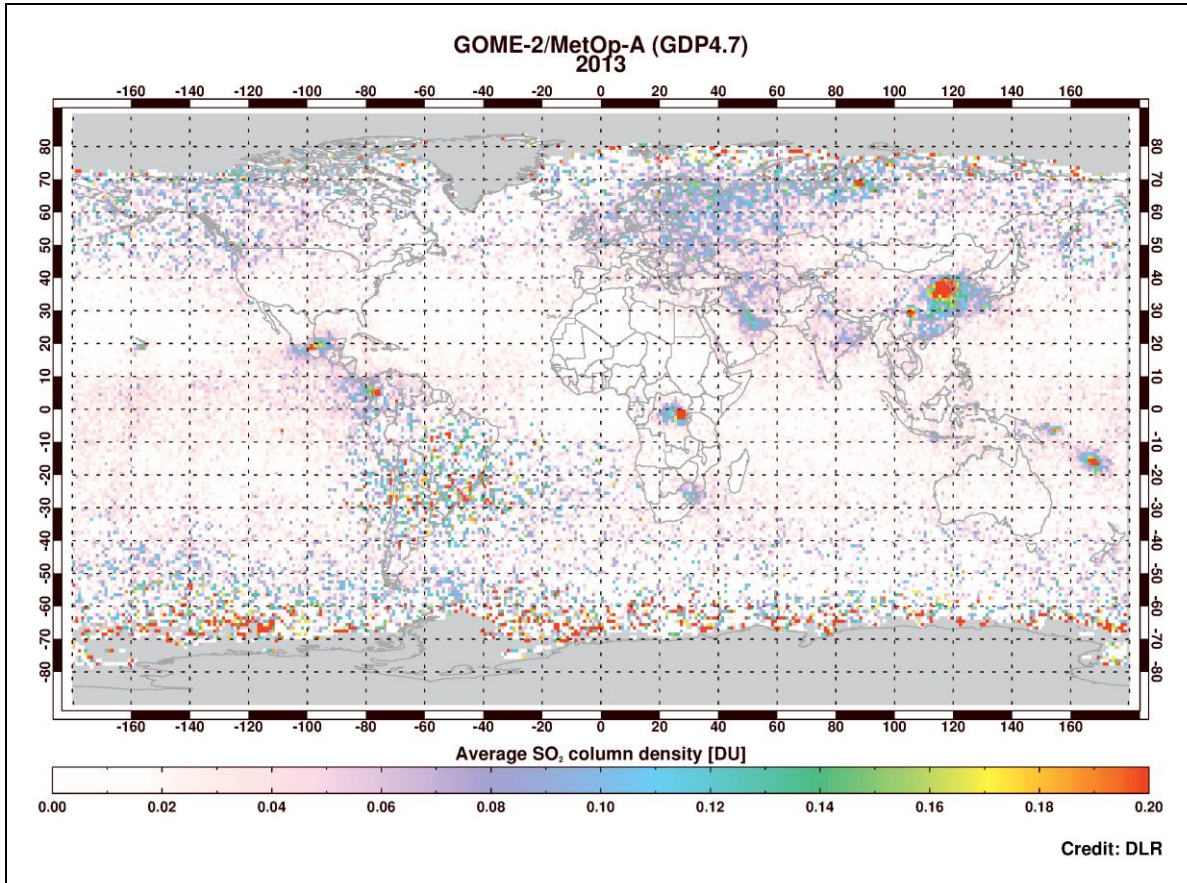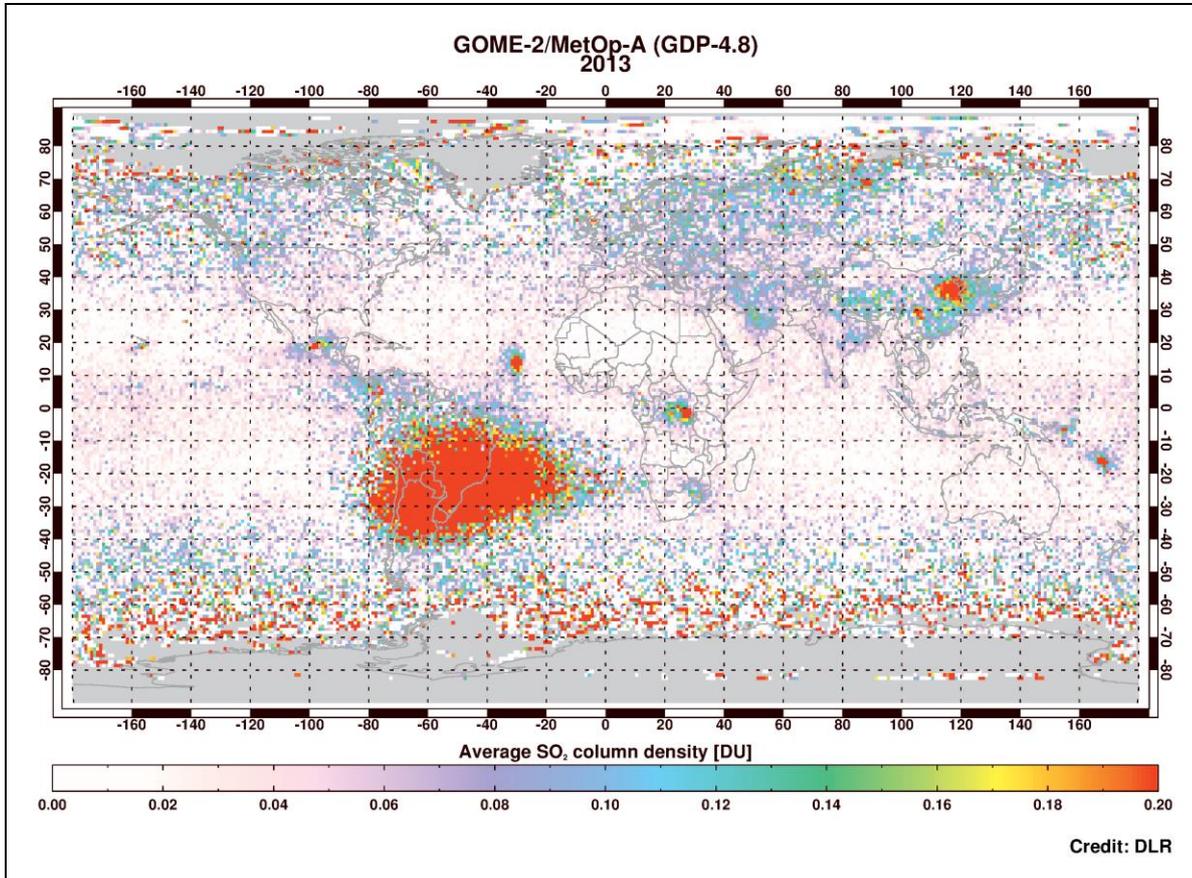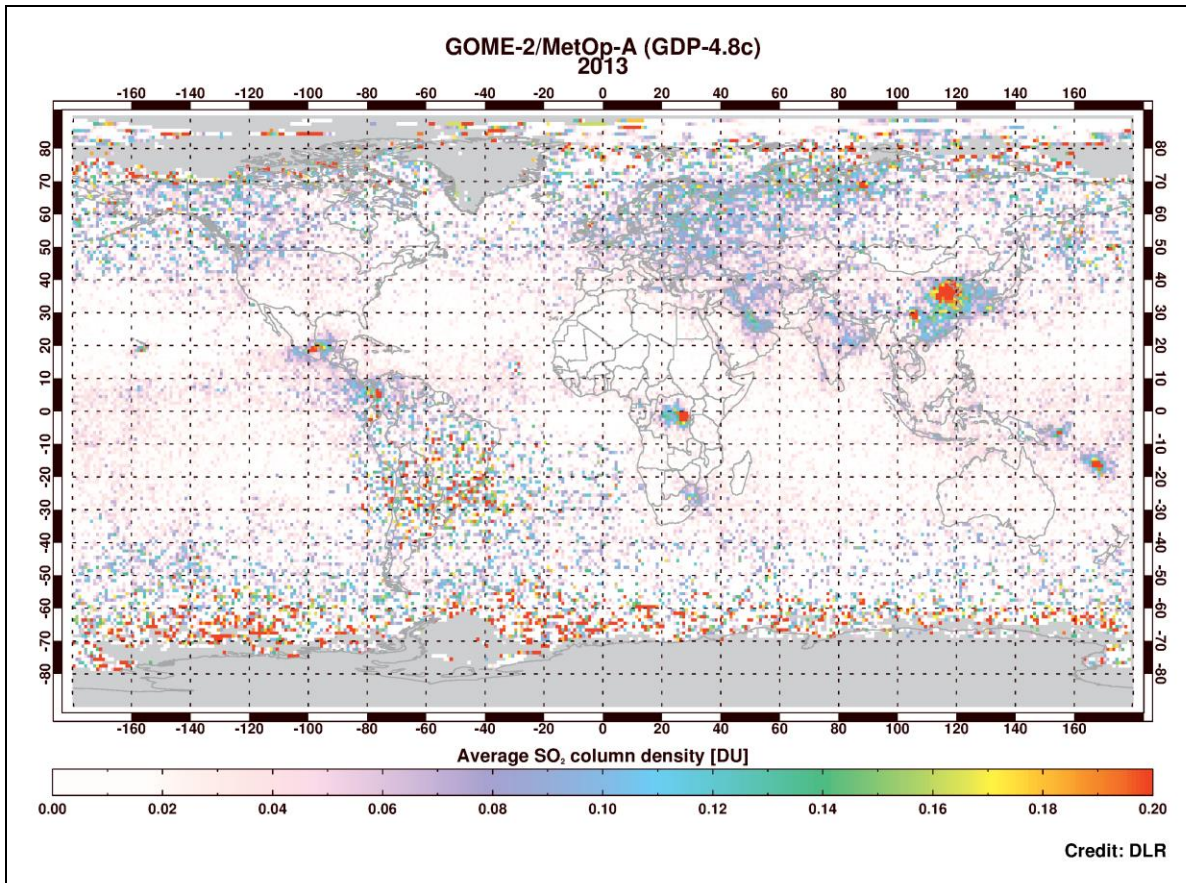
Figure 10. Global SO$_2$ VCD for the volcanic product at 15km for GOME-2A. **Top:** GDP4.7 algorithm. **Middle:** GDP4.8 algorithm validated in this report. **Bottom:** Test GDP4.8 algorithm run using the inverted Solar spectrum.

In Figure 10 the effect of fitting an Inversed Solar irradiance spectrum in the GOME-2A data is demonstrated for the GDP4.7 algorithm [upper panel], the GDP4.8 algorithm [middle panel] and the new test settings of GDP 4.8 algorithm [lower panel.] Hence, for both GDP4.7 [upper] and the new test setting of GDP4.8 [lower] the GOME-2A data were fitted with an Inversed Solar irradiance spectrum, whereas for the GDP 4.8 under validation in this report [middle] an Inversed Earthshine spectrum was used.

Even pictorially, the increase in the noise levels in the middle panel of Figure 10 is unmistakable on a global scale, with spurious features appearing [such as the high positive SO$_2$ loadings at -30°W and 15°N] on top of that. The application of the Inversed Solar irradiance on the GDP4.8 algorithm for GOME-2A makes the picture quite similar to the original GDP4.7 version [top panel.]

Conversely, for GOME-2B, no major differences can be seen when moving from GDP4.7 to GDP4.8 [top and middle panel of Figure 11] whereas an improvement can be noted in the move to the new test run of GDP4.8 [bottom panel of Figure 11].

GOME-2/MetOp-B (GDP4.7)
2013

Average SO₂ column density [DU]

Credit: DLR

GOME-2/MetOp-B (GDP-4.8)
2013

Average SO₂ column density [DU]

Credit: DLR
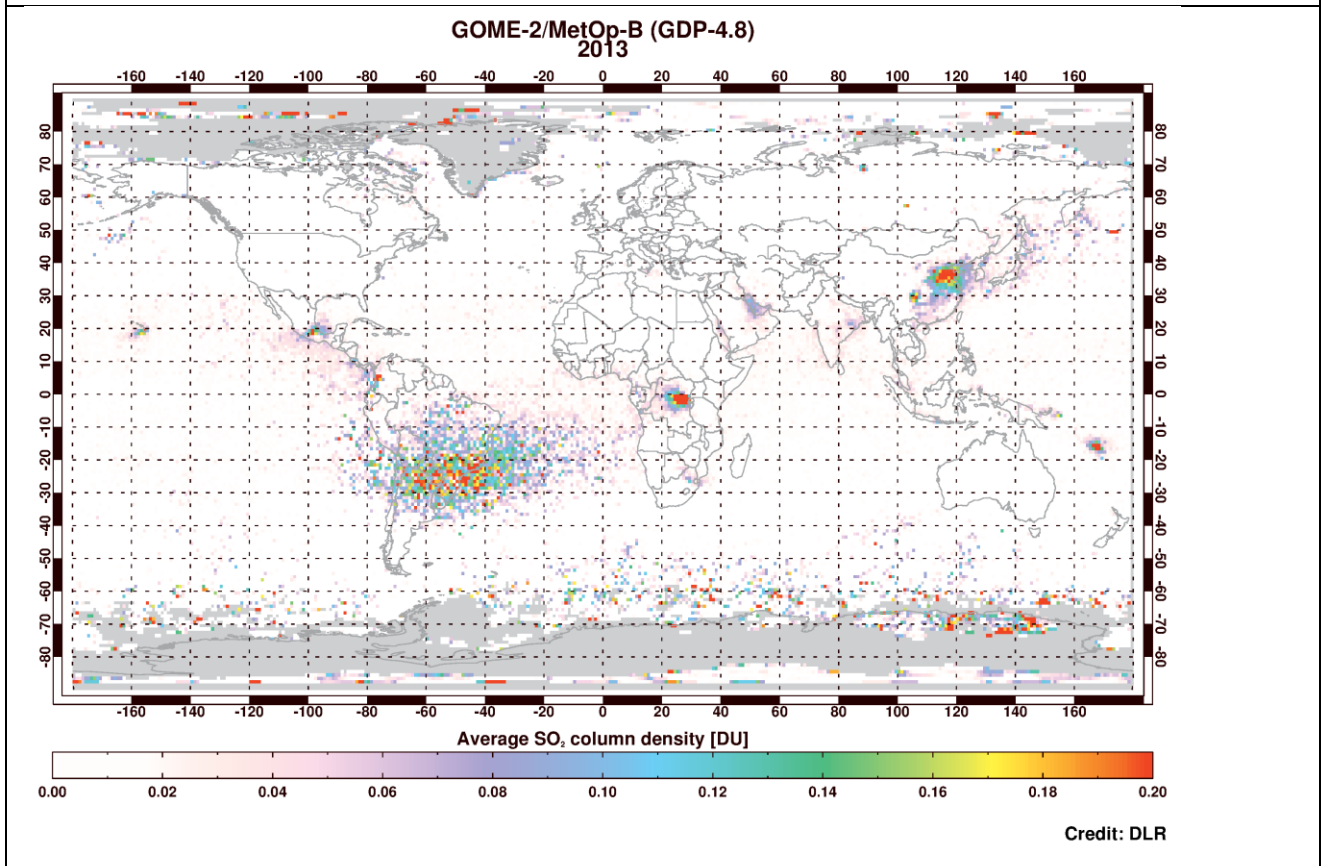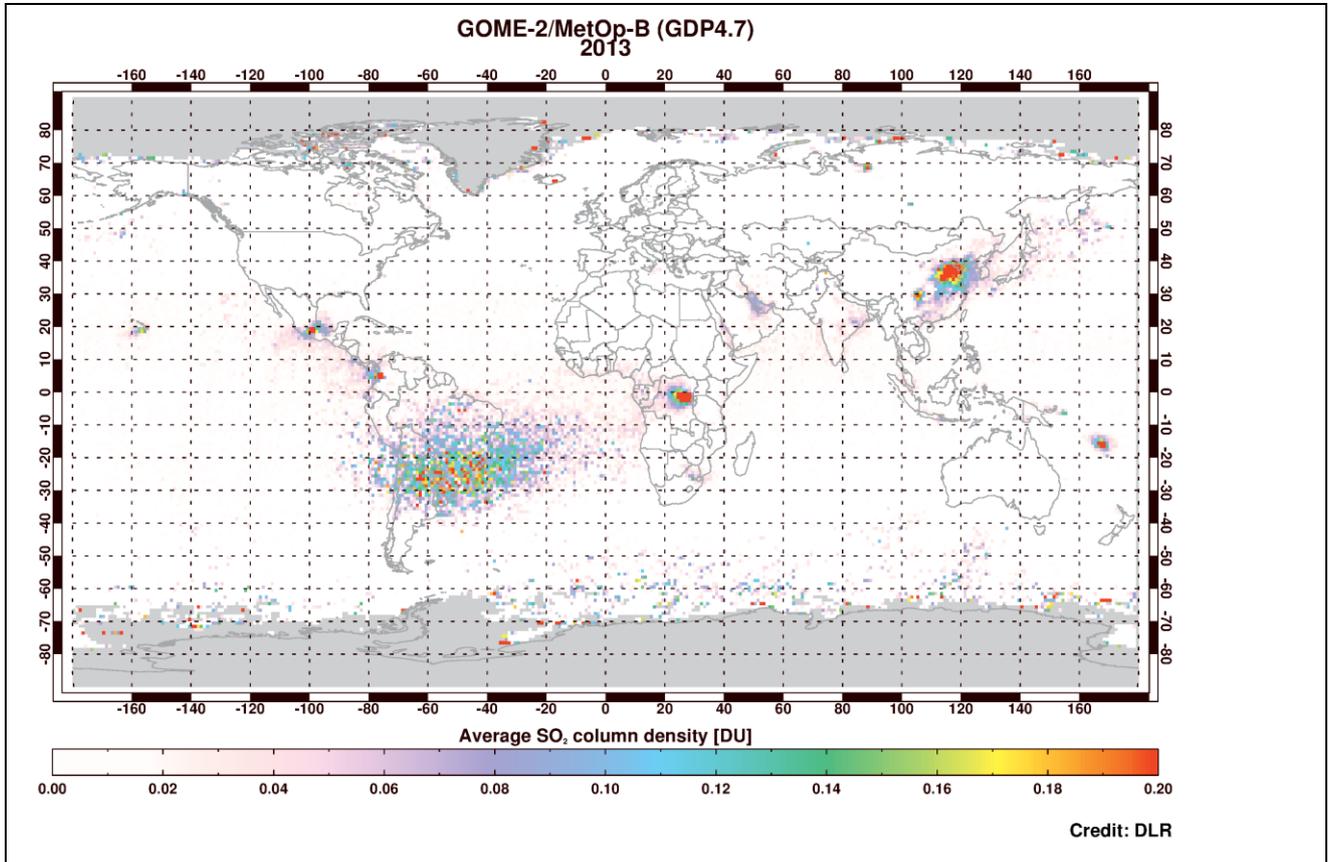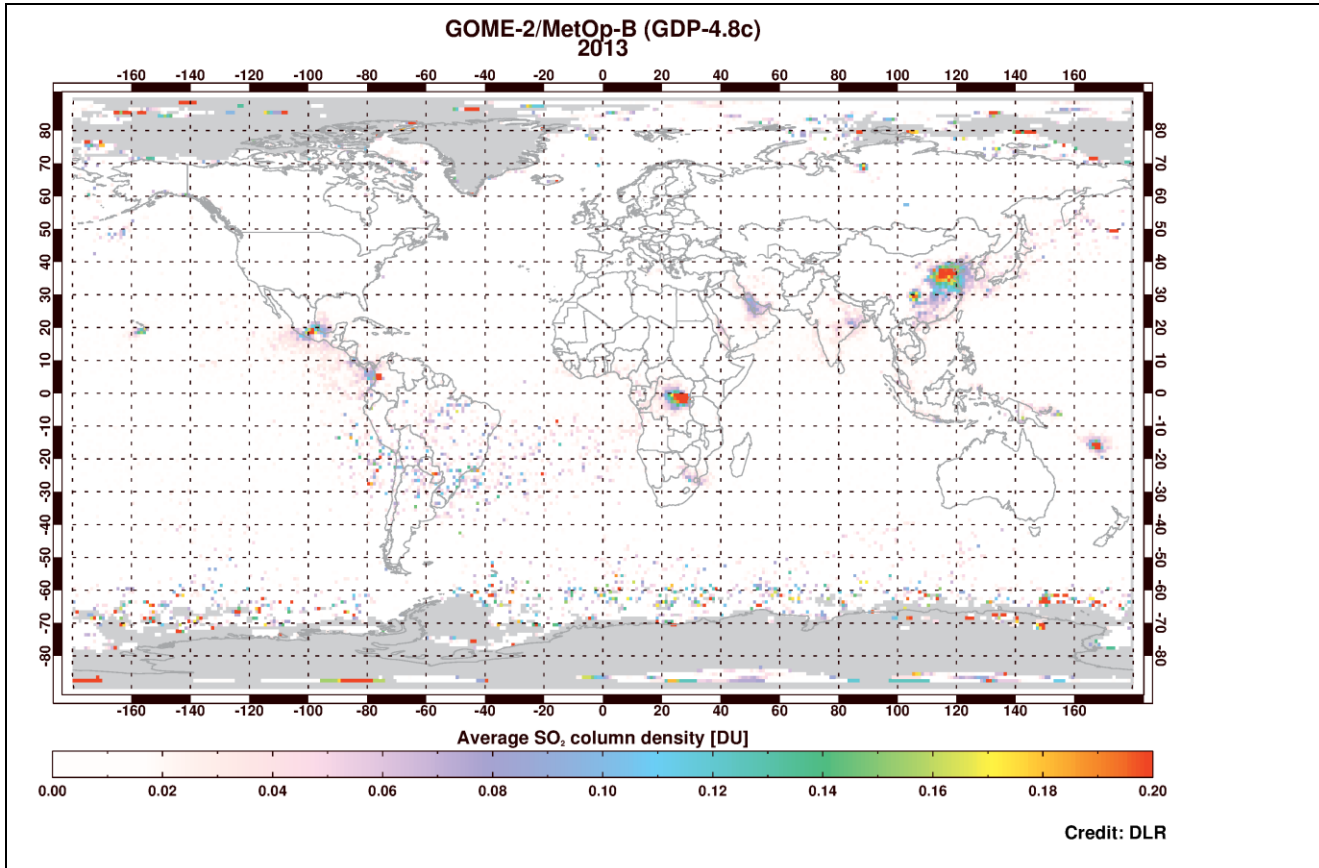
Figure 11. Global SO₂ VCD for the volcanic product at 15km for GOME-2A. **Top:** GDP4.7 algorithm. **Middle:** GDP4.8 algorithm validated in this report. **Bottom:** Test GDP4.8 algorithm run using the inverted Solar spectrum.

Quite similarly, as was shown in Figures Figure 10 and Figure 11 for the volcanic product, we show in Figure 12 the anthropogenic product at 2.5km for GOME-2A [upper] and GOME-2B [lower] for the new test settings of GDP4.8. The differences between the two instruments are quite distinct, with GOME-2A suffering not only from the higher noise levels, which sometimes reach the levels of known hot-spots, but also in the location and extend of said known hot-spot regions.

GOME-2/MetOp-A (GDP-4.8c)
2013
Average SO₂ column density [DU]
Credit: DLR

GOME-2/MetOp-B (GDP-4.8c)
2013
Average SO₂ column density [DU]
Credit: DLR
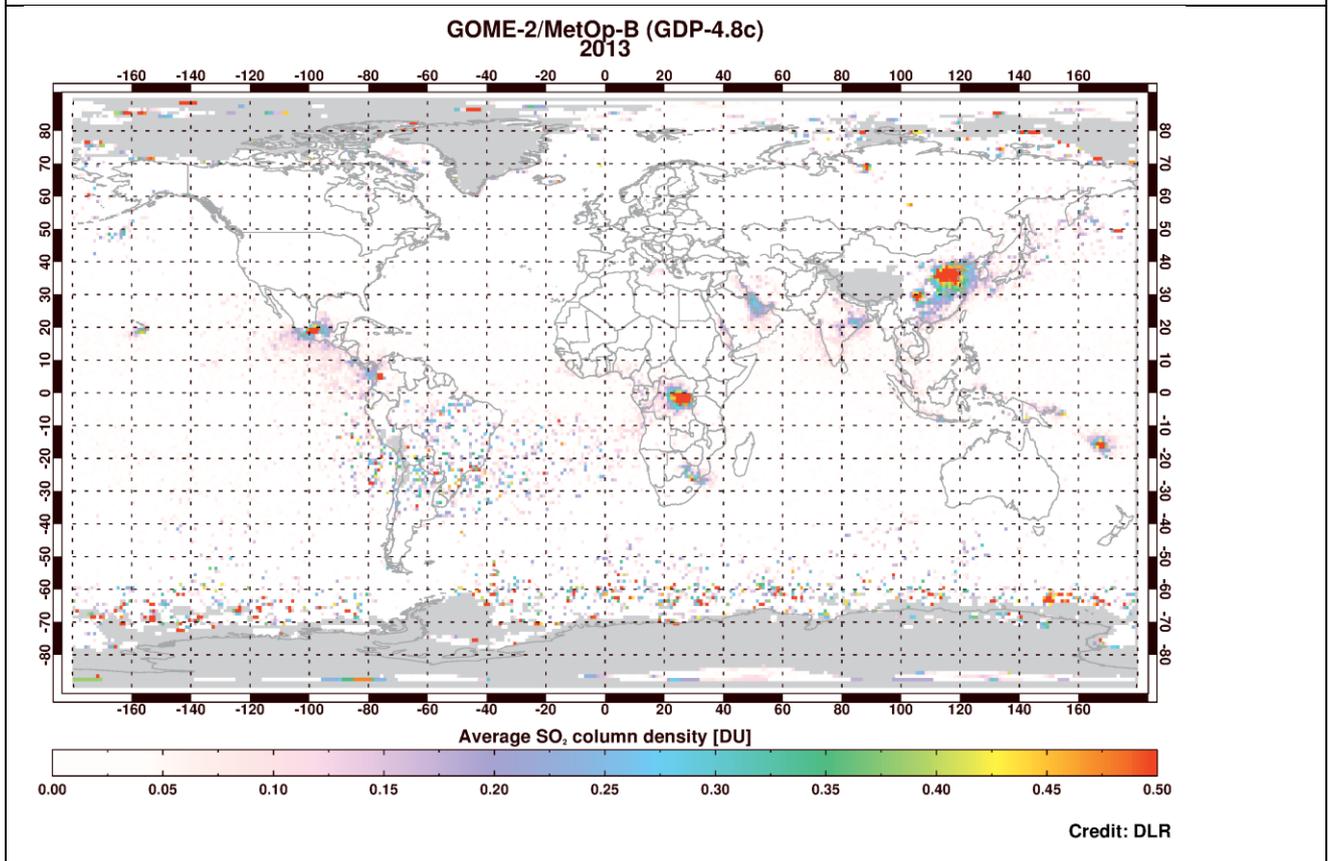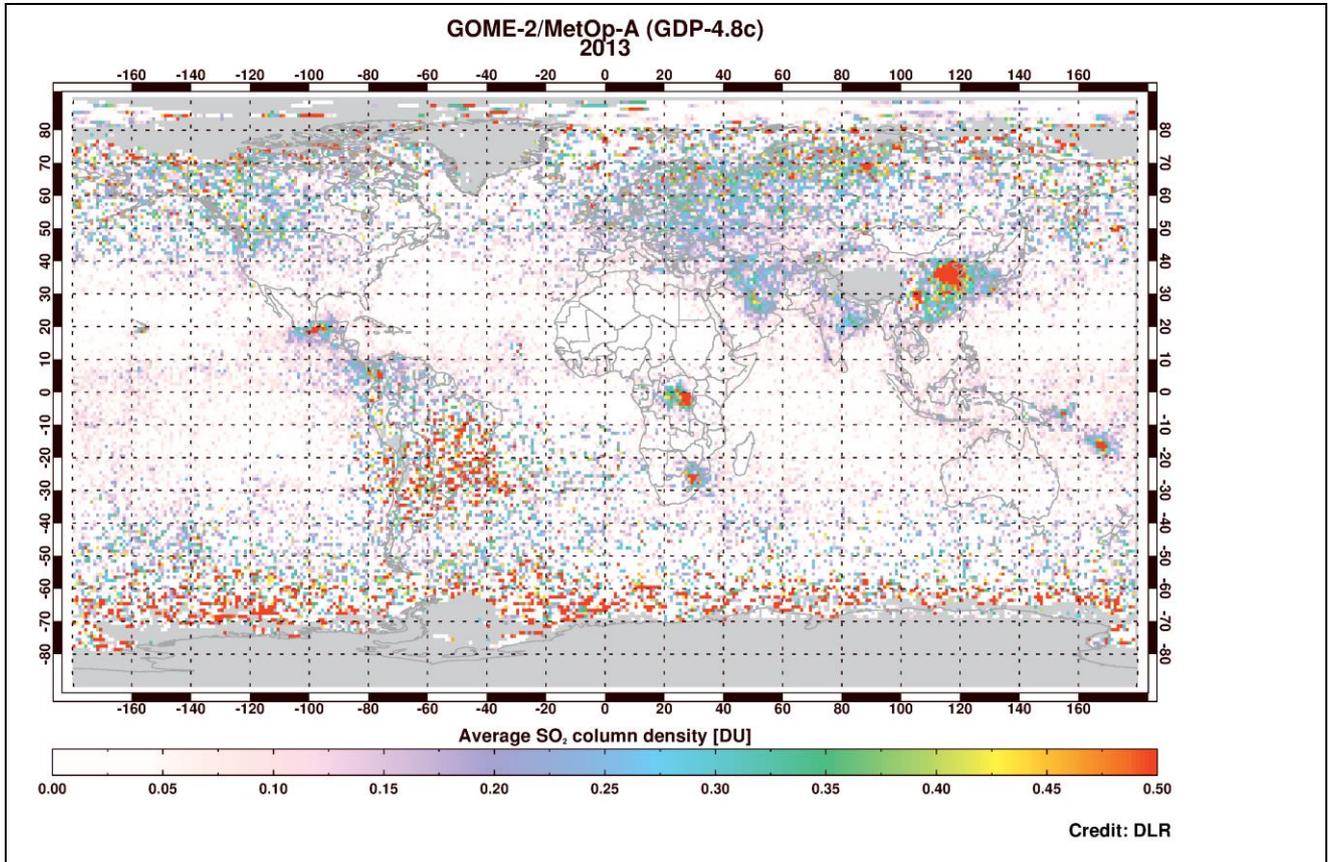
Figure 12. Global SO_2 VCD for the anthropogenic product at 2.5km for GOME-2A [upper] and GOME-2B [lower] for the test GDP4.8 algorithm run using the inverted Solar spectrum.

C.1.3 Comparisons between total SO_2 columns seen by the GOME-2 MetOp-A and -B instruments and the OMI/Aura datasets

In Figure 13, the GDP4.8 1km product is now compared to the OMI NASA SO_2 load. GOME-2A is shown on the upper left and GOME-2B on the upper right and the OMI product at the bottom. The two instruments do differ in GDP4.8 both in the background values and the hotspot magnitude, albeit with smaller differences that in GDP4.7. In Figure 14 the differences between GOME-2A and GOME-2B against the OMI data are shown. The GOME-2B differences (right) are larger in magnitude and affect both the background and the hotspots, showing a GOME-2B under-estimation against OMI which is not repeated in the GOME-2A maps (left).
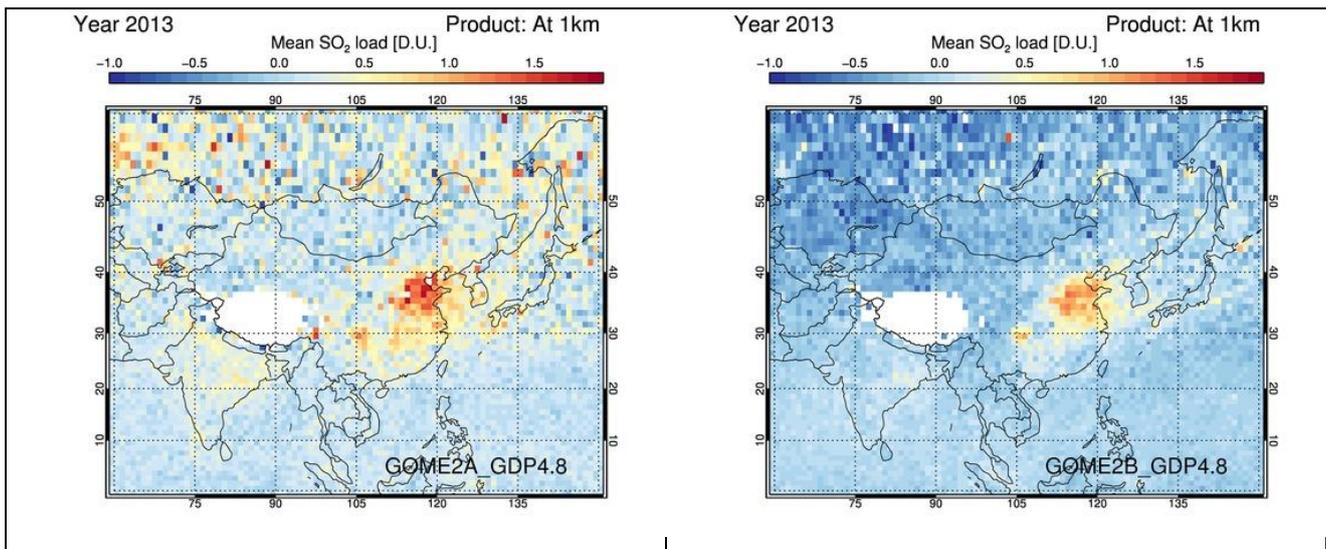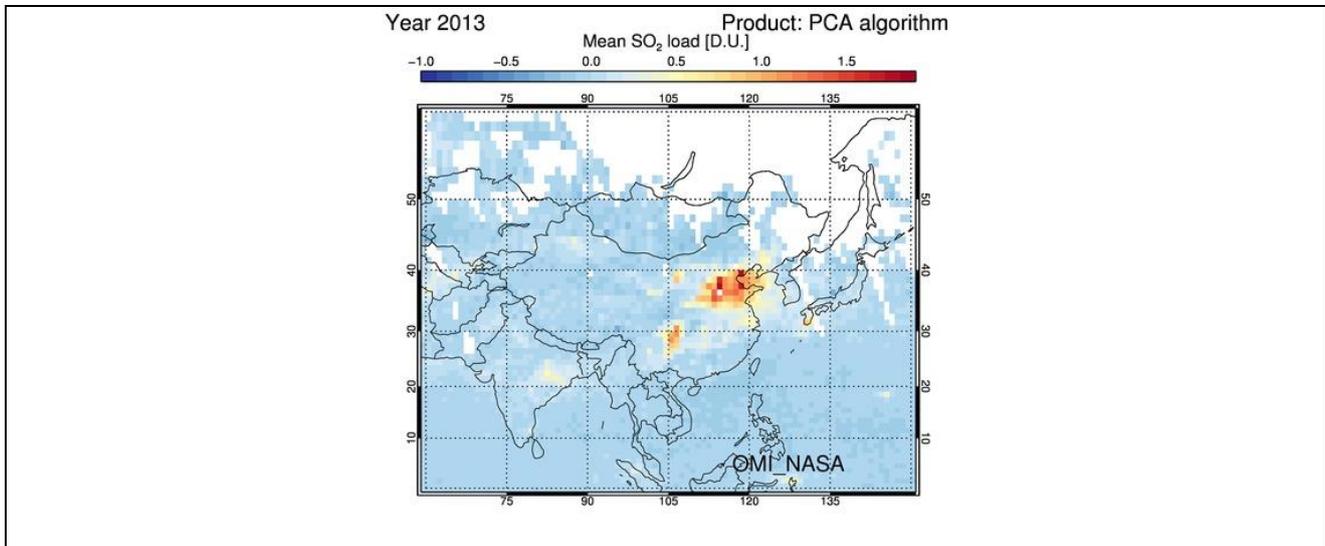
Figure 13: Comparison between the GOME-2A GDP4.8 [upper left] mean SO$_2$ loading and GOME-2B GDP4.8 [upper right] and OMI_NASA [lower]. For year 2013 and the 1km product.
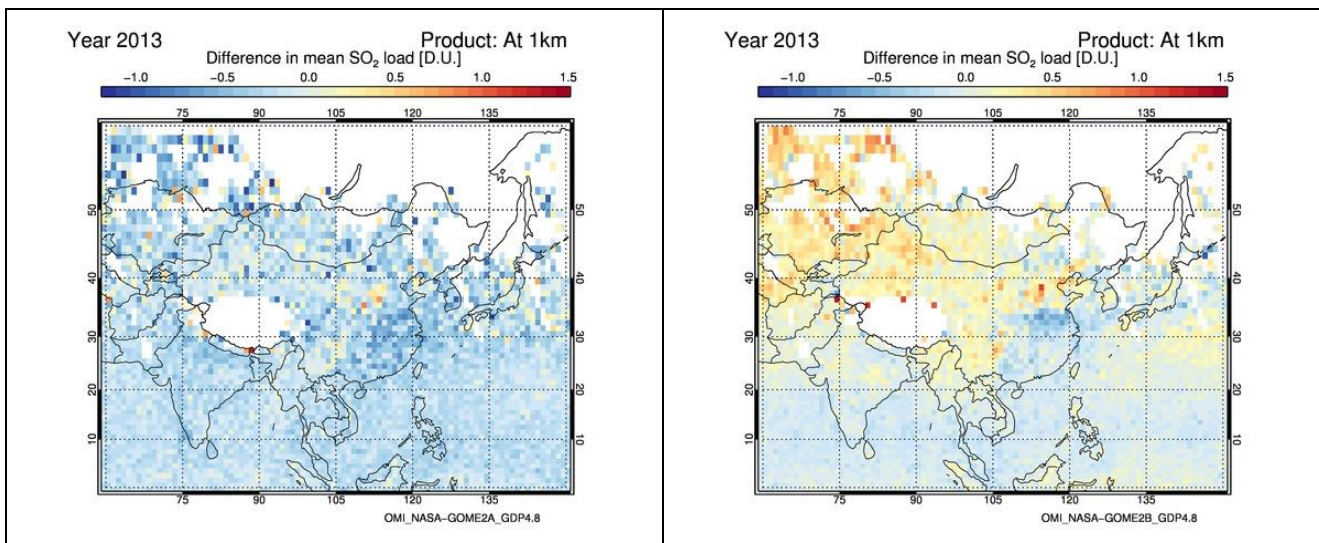
**Figure 14**: The differences of the maps shown in Figure 13, on the left the difference between GOME-2A GDP4.8 and OMI and on the right, GOME-2B GDP4.8 and OMI for year 2013 and the 1km product.

In Table II a list of known SO$_2$ emitting locations on a global scale are given, sorted in latitude. These include volcanoes, as natural SO$_2$ sources, and power plants/smelters/oil industry locations, as anthropogenic SO$_2$ sources. For these locations, a detailed investigation was performed for both the 1km and the 2.5km GDP4.8 product and parts of it are shown below. Recall that this analysis is now performed on a grid closer to the actual satellite footprint, of 0.25°x0.25°. An example of three locations in a yearly average for 2013 is presented in Figure 15 with a volcano in Vanuatu shown at the top, oil industry pollution in Saudi Arabia in the middle and smelter activity in Siberia at the bottom row. As can be seen, even though the spatial resolution may decrease in the area weighted mean product (right column) the noise levels also decrease appreciably compared to the simple mean on the grid cells (left column) and enable a quantitative comparison between algorithms presented further down excluding irrelevant cells.
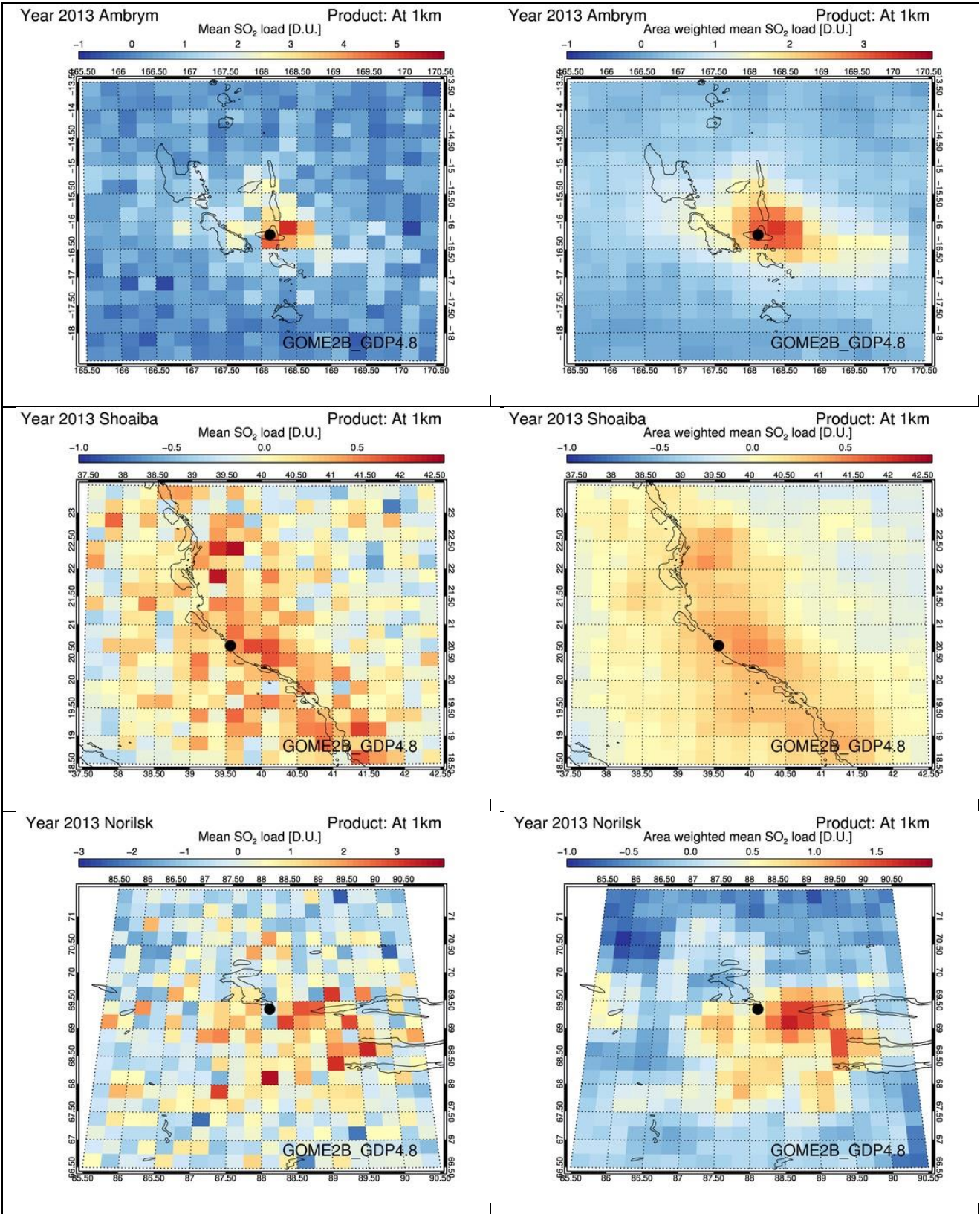
Figure 15. Examples of the SO$_2$ loading around some of the locations listed in Table II as seen by the GOME-2B GPD4.8 1.km product. A volcano in Vanuatu is shown at the top, oil industry pollution in Saudi Arabia in the middle and smelter activity in Siberia at the bottom row. The simple mean data are shown on the left and the area weighted average data on the right column.

In Figure 16 scatter plot comparisons based on the 0.25°x0.25° area weighted maps are presented for the year 2013 and for the 1km product. In order to try and filter out noisy data, a threshold is applied where a daily 0.25°x0.25° grid mean VCD observation is allowed to continue into the creation of the monthly 0.25°x0.25° grids only if it is larger than twice the 1-sigma of the mean. Hence in the left column the non-filtered data are shown and in the right column the filtered data. The OMI_NASA product is used as "truth", and always appears on the x-axis. From top to bottom: Eastern China multiple sources, Manam Volcano and the Nyiragongo - Nyimaruagira Volcanic complex, in the Congo. In general, the un-filtered data in the left column appear to show larger correlation coefficients [see top left corner of all graphs] than the un-filtered data in the right column. In the text below, the un-filtered comparisons in the left will be discussed further.

All locations show a very good agreement between the two types of sensors, with high correlation coefficients, and a near-constant overestimation of GOME-2A compared to GOME-2B for all OMI coincidences [or under-estimation of GOME-2B compared to GOME-2A.] In more detail, the Eastern China location, top row, has a correlation coefficient of 0.822 for GOME-2B and 0.785 for GOME-2A; the Manam Volcano, 0.622 and 0.611 respectively, and the Nyiragongo Volcano a spectacular 0.962 for both sensors.
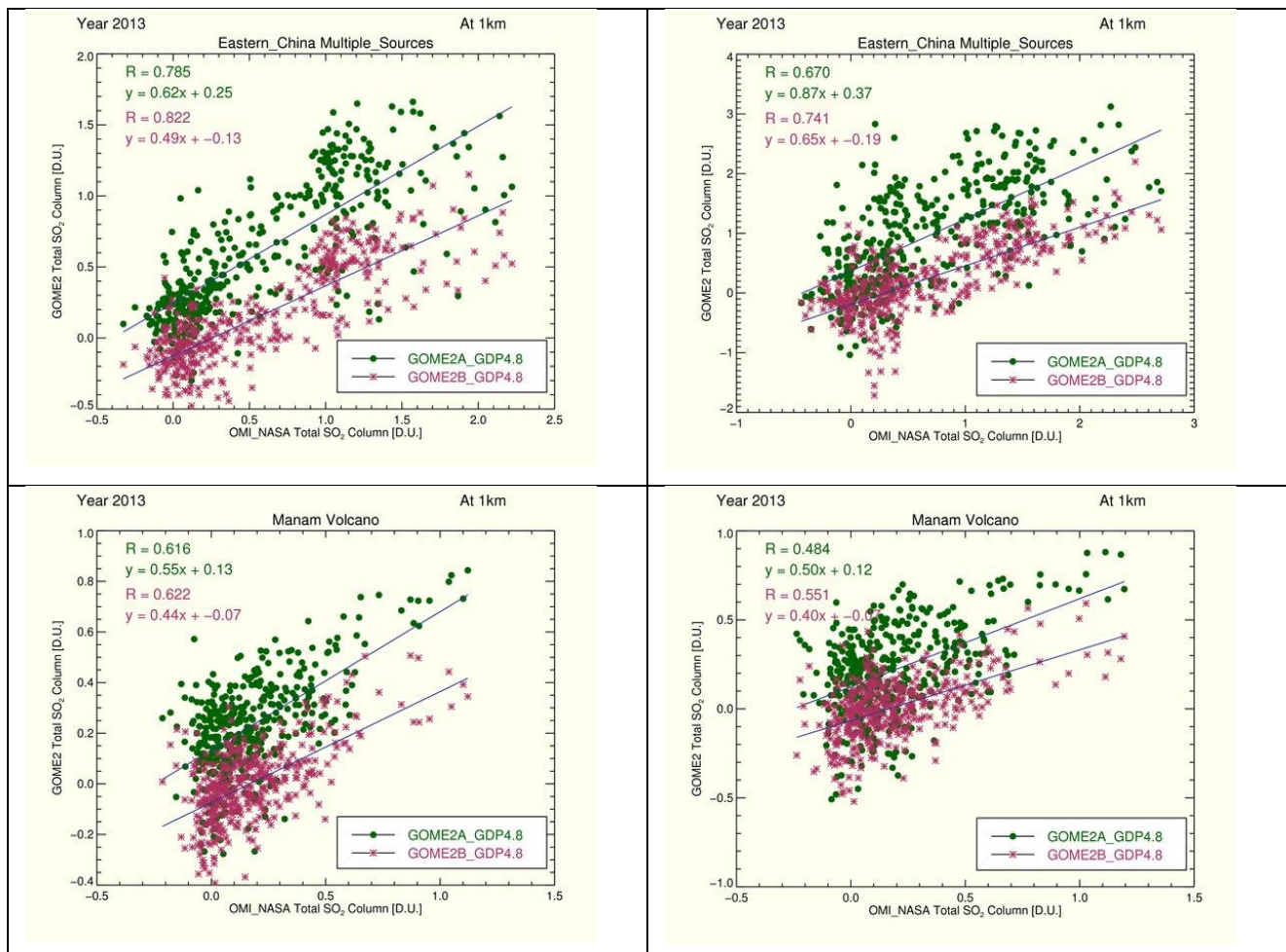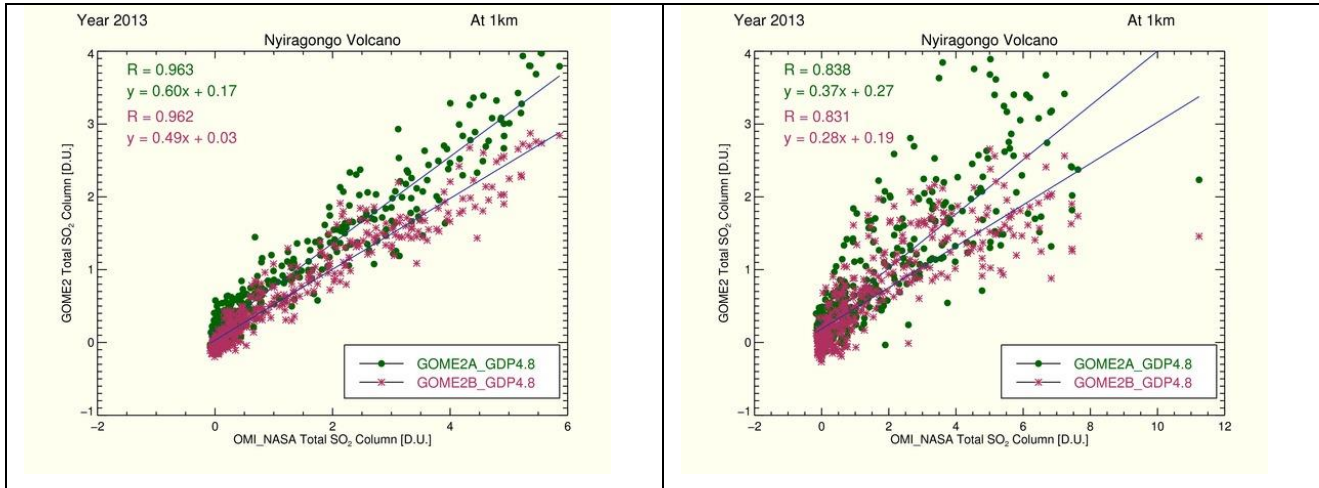
Figure 16: Scatter plots between the 2013 OMI/Aura NASA PCA SO₂ columns (x-axis) and the GOME-2A (green) & GOME-2B (purple) GDP4.8 SO₂ columns at 1km (y-axis) at selected locations: Eastern China, Manam volcano in Papua, New Guiney, and the Nyiragongo volcano in the Congo. The statistic parameters are also given inset. <u>Left column</u>: non-filtered data. <u>Right column</u>: grid mean value included in the comparisons if is larger than twice the 1-sigma of the mean.

Table III. Statistics [r-squared and slope] for the comparisons between GOME-2A and GOME-2B GDP4.8 1km product against the OMI PCA product show in the left column of Figure 16.

Name	Source type	GOME-2A GDP4.8 vs OMI R²		GOME-2A GDP4.8 vs OMI slope		GOME-2B GDP4.8 vs OMI R²		GOME-2B GDP4.8 vs OMI slope	
Nyiragongo	Volcano	0.96		0.6		0.96		0.49	
Kilauea_Hawaii	Volcano	0.92		0.46		0.95		0.41	
Ambrym	Volcano	0.9		0.6		0.84		0.48	
Bagana	Volcano	0.81		0.52		0.84		0.44	
Eastern_China	Multiple_Sources	0.79		0.62		0.82		0.49	
Tula_Popocatepetl	Industrial_Volcano	0.77		0.39		0.87		0.44	
Turvurvur_Rabaul	Volcano	0.68		0.49		0.67		0.39	
Oil_Fields_in_Gulf_of_Mexico	Oil_Industry	0.67		0.73		0.79		0.65	
Shoaiba	Oil_Industry	0.65		0.61		0.76		0.64	
East_Java	Volcano	0.64		0.65		0.65		0.58	
Manam	Volcano	0.62		0.55		0.62		0.44	
Dukono	Volcano	0.62		0.55		0.69		0.46	
Khark_Island	Oil_Industry	0.61		0.82		0.75		0.7	
Manzanillo	Power_Plants	0.52		0.38		0.66		0.47	
Sarcheshmeh	Smelter	0.45		0.46		0.42		0.24	

Shizuishan	Multiple_Sources	0.42		0.46		0.58		0.35	
South_Africa	Power_Plants	0.32		0.39		0.38		0.32	
Anatahan	Volcano	0.29		0.27		0.63		0.5	
Mayon	Volcano	0.2		0.45		0.27		0.51	
Guangdong	Multiple_Sources	0.2		0.53		0.31		0.54	
Lewotolo	Volcano	0.18		0.31		0.43		0.5	
Copahue	Volcano	0.15		0.34		0.053		0.093	
Mt_Etna	Volcano	0.14		0.16		0.43		0.49	
Marica	Power_Plants	0.14		0.55		0.14		0.32	
Soufriere_Hills	Volcano	0.11		0.26		0.24		0.39	
Miyakejima	Volcano	0.11		0.51		0.45		1.33	
Balqash	Smelter	0.11		0.25		-0.19		-0.43	
Norilsk	Smelter	0.11		0.06		-0.06		-0.027	
Balkans	Power_Plants	0.043		0.07		0.27		0.33	
Ilo_Ubinas	Smelter_Volcano	0.027		0.09		0.13		0.29	
Rovinary_Turceni_Isalnita	Power_Plants	-0.1		-0.2		0.38		0.6	

In Table III, the comparative statistics for all locations analysed are given, sorted by the highest R-squared correlation coefficient between GOME-2A GDP4.8 1km product and OMI PCA algorithm product [third column.] The equivalent slope of the fit is given in the fourth column, whereas the same by for GOME-2B are presented in columns five and six. One may conclude that overall the GOME-2A and GOME-2B–B agree reasonably well on average for good correlations with OMI [down to an r-squared of 0.50, which represents more than half the locations shown.] This mediocre overall correlation finding may be partly attributed to the relatively large scatter of GOME-2 data and to the better spatial resolution of OMI. The slope of the regression lines for both GOME-2A and GOME-2B vs OMI are systematically lower than one, suggesting a difference in assumptions of the radiative transfer calculations. One of the most probable differences of those assumptions/choices is the use of AMF to move from the slant column density to the vertical column density. The OMI PCA algorithm uses a constant, single, clear-sky AMF of 0.36 to transform to VCDs. The choice of clear or total AMF in the GDP4.8 algorithm is hence an important factor to look into.

Strong sources such as volcanoes but also important anthropogenic locations feature with high correlations in Table III, with the surprising exception of the smelters in Norilsk, Siberia, which are considered a major source of anthropogenic SO_2 easily identifiable from space and publications using both OMI/Aura and IASI/MetopA exist. In Table IV the mean and standard deviation for the locations discussed in Table III are given, sorted as per Table III. It may be noted that, for most locations, the higher correlations are found for the strongest sources, a fact that is further attested to by Figure 17where the correlation coefficient r-squared between GOME2 and OMI [x-axis] is compared to the mean GOME2 VCD [y-axis]. In red, the 1km product and in blue, the 2.5km product comparisons are given [not shown above.] On the left, for GOME-2A, no correlation can be seen between the magnitude of the SO_2 source and the correlation to OMI, whereas for GOME-2B on the right, a quite interesting correlation is seen for both the 1km and the 2.5 km product. This fact points further to the discrepancies between the SO_2 columns reported by GOME-2A and GOME-2B and the superiority of GOME-2B probably due to the smaller degradation effects in year 2013. The clear

distinction between the magnitude of values of two SO$_2$ columns [1km and 2.5km] for the GOME-2B compared to GOME-2A is also well-depicted in these comparisons.
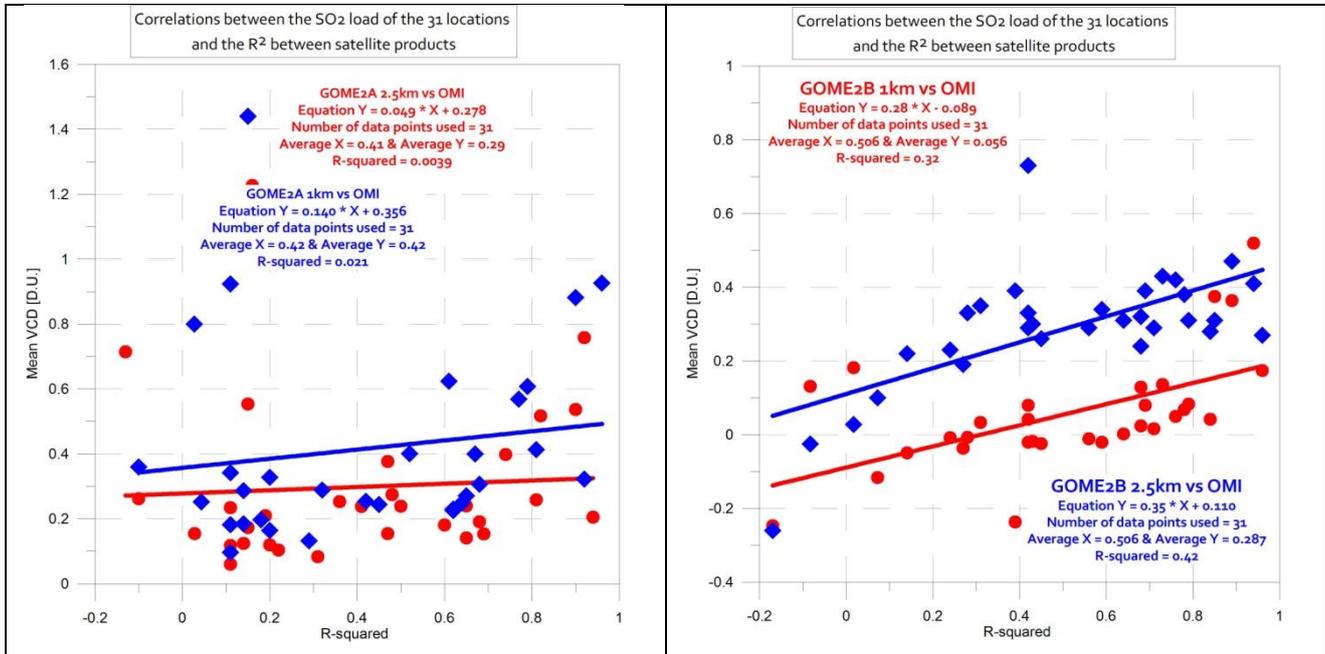

Figure 17. Scatter plots between the GOME2 mean VCD value [y-axis] and R-squared of the GOME2 vs OMI comparisons [x-axis] for the 31 locations discussed in Table III and Table IV. On the left, the GOME-2A comparisons and on the right, the GOME-2B comparisons; with red, the 1km GOME2 product and with blue, the 2.5 km GOME2 product are given. The statistics of this comparison are inset.

Table IV. The mean and standard deviation in [D.U.] of the GOME-2A GDP4.8, GOME-2B GDP4.8 and OMI/NASA locations sorted as per Table III for ease of read.

Name	Source type	GOME -2A mean and std				GOME-2B mean and std				OMI mean and std		
Nyiragongo	Volcano	0.926	±	0.925		0.649	±	0.757		1.27	±	1.495
Kilauea_Hawaii	Volcano	0.323	±	0.353		0.289	±	0.305		0.425	±	0.704
Ambrym	Volcano	0.882	±	0.679		0.623	±	0.576		1.1	±	1.007
Bagana	Volcano	0.413	±	0.263		0.073	±	0.215		0.304	±	0.405
Eastern_China	Multiple_Sources	0.608	±	0.455		0.16	±	0.344		0.582	±	0.574
Tula_Popocatepetl	Industry/Volcano	0.569	±	0.406		0.399	±	0.401		1.046	±	0.795
Turvurvur_Rabaul	Volcano	0.307	±	0.193		0.047	±	0.153		0.214	±	0.266
Gulf_of_Mexico	Oil_Industry	0.4	±	0.241		0.121	±	0.18		0.172	±	0.219
Shoaiba	Oil_Industry	0.271	±	0.17		0.092	±	0.152		0.144	±	0.182
East_Java	Volcano	0.249	±	0.17		0.14	±	0.148		0.146	±	0.166
Manam	Volcano	0.23	±	0.192		0.002	±	0.153		0.175	±	0.216
Dukono	Volcano	0.226	±	0.171		0.037	±	0.128		0.118	±	0.192
Khark_Island	Oil_Industry	0.624	±	0.268		0.253	±	0.188		0.301	±	0.199

Manzanillo	Power_Plants	0.401	±	0.183		0.217	±	0.183		0.409	±	0.253
Sarcheshmeh	Smelter	0.244	±	0.192		-0.020	±	0.108		0.153	±	0.187
Shizuishan	Multiple_Sources	0.254	±	0.264		-0.022	±	0.147		0.192	±	0.242
South_Africa	Power_Plants	0.289	±	0.427		0.092	±	0.291		0.342	±	0.349
Anatahan	Volcano	0.132	±	0.096		0.013	±	0.082		-0.015	±	0.103
Mayon	Volcano	0.164	±	0.119		-0.0043	±	0.103		-0.030	±	0.053
Guangdong	Multiple_Sources	0.328	±	0.219		0.0533	±	0.14		0.0050	±	0.080
Lewotolo	Volcano	0.197	±	0.171		-0.0259	±	0.118		0.0185	±	0.1
Copahue	Volcano	1.44	±	0.591		-0.172	±	0.474		0.271	±	0.27
Mt_Etna	Volcano	0.287	±	0.223		-0.0173	±	0.233		0.151	±	0.205
Marica	Power_Plants	0.185	±	0.311		-0.065	±	0.183		0.0595	±	0.077
Soufriere_Hills	Volcano	0.097	±	0.108		-0.003	±	0.073		-0.0375	±	0.045
Miyakejima	Volcano	0.182	±	0.279		0.0755	±	0.184		0.0671	±	0.062
Balqash	Smelter	0.342	±	0.177		-0.347	±	0.178		0.0127	±	0.080
Norilsk	Smelter	0.924	±	0.423		0.245	±	0.363		1.51	±	0.79
Balkans	Power_Plants	0.252	±	0.248		-0.0455	±	0.175		0.094	±	0.145
Ilo_Ubinas	Smelter_Volcano	0.8	±	0.568		0.19	±	0.376		0.0238	±	0.167
Rovinary_Turceni_Isalnita	Power_Plants	0.36	±	0.268		-0.334	±	0.194		0.0642	±	0.124

C.1.4 Conclusions from Section C.1

From the results presented in this section we may reach the following conclusions, keeping in mind that the main aim of this validation report is to assess the quality of the new GDP4.8 algorithm on both GOME-2A and GOME-2B observations.

- ▪ GOME-2A GDP4.8 2.5km plume height product shows higher SO_2 estimates, including pronounced SSA regions issues that do not appear in GDP4.7, for the beginning of the mission in the least. For year 2013, these SAA issues are shown in both GDP4.7 and GDP4.8. Test runs for years 2008 and 2013 have shown that the differences, between both the GDP versions, introduced by differences in the intensity offset correction explain this feature.

- ▪ GOME-2A GDP4.8 2.5km plume height product shows between 0 and 0.5-1 D.U. higher SO2 loading on a yearly basis than the GDP4.7 algorithm, whereas for GOME-2B this increase is smaller, between 0 and 0.5 D.U. at the known hot spots.

- ▪ When comparing directly slant column densities instead of vertical column densities between the two algorithms, for GOME-2B it is found that the small [between 0 and 0.2 D.U.] difference may be attributed to the new AMF calculation that contains a novel cloud treatments function. For GOME-

2A the SCD differences are rather large, up to 0.5. D.U., and their attribution remains work in progress.

- The new GOME-2A GDP4.8 1km anthropogenic SO_2 product is far noisier, even on a yearly mean basis, than the traditional 2.5km product, with all well-known global hotspots appearing clearer and with higher loadings. For GOME-2B the picture is more delicate since more negative values appear in the background locations on a global scale for this product.

- When comparing the new GOME-2A and GOME-2B 1km product with the OMI/Aura equivalent, it is found that the GOME-2B differences are larger in magnitude and affect both the background SO_2 field as well as the hotspots, showing a GOME-2B under-estimation against OMI which is not repeated in the GOME-2A maps.

- When focusing on specific locations around the world, with known, or expected, high SO_2 loadings of both anthropogenic and natural source, it is found that all locations show a very good agreement between the two types of sensors, with high correlation coefficients, and a near-constant overestimation of GOME-2A compared to GOME-2B for all OMI coincidences [or under-estimation of GOME-2B compared to GOME-2A.]

- For most locations, the higher correlations are found for the strongest sources. However, when comparing the correlation coefficient r-squared between GOME2 and OMI to the mean GOME2 VCD for GOME-2A, no correlation can be seen between the magnitude of the SO_2 source and the correlation to OMI, whereas for GOME-2B on the right, a quite interesting correlation is seen for both the 1km and the 2.5 km product. This fact points further to the discrepancies between the SO_2 columns reported by GOME-2A and GOME-2B and the superiority of GOME-2B probably due to the smaller degradation effects in year 2013.

C.2 Verification of SO$_2$ vertical columns for specific volcanic eruptions and anthropogenic SO$_2$ over China

C.2.1 Volcanic SO$_2$

In the present study, the approach that has been adopted is to verify/validate the GOME-2A and -B SO$_2$ products through cross-comparisons with the OMI SO$_2$ product of Theys et al. (2015), which itself has been extensively compared with other satellite measurements from IASI/MetopA and OMI/Aura (NASA algorithms). However, it should be noted that this approach poses a number of problems since Aura has a different overpass time than MetopA and MetopB and dissimilar swath and spatial resolution than the GOME-2 sensors. Hence, as a workaround, we have compared only the total SO$_2$ masses. As a baseline, we have assumed a single SO$_2$ plume height (15km) consistently for all instruments. For the cases below, it is understood that the actual SO$_2$ plume heights are different than the assumed height. Therefore the estimated masses are likely to be somewhat different than the actual ones, but since both data sets (OMI, GOME-2) are affected in the similar way this effect is minimized.

As a first test case, we investigate the SO$_2$ results for the eruption of Kasatochi, Alaska, that started on 7-8 August 2008. The SO$_2$ plume could be detected by GOME-2 for many weeks after the start of the eruption as the plume dispersed throughout the whole Northern hemisphere. There is no need to demonstrate the ability of GOME-2 to locate the SO$_2$ plume as it is clear from the SO$_2$ maps generated by the SACS system (sacs.aeronomie.be) that GOME-2 captures similar patterns as other sensors such as AIRS/Aqua, OMI/Aura and IASI/MetopA. However, the GDP4.8 SO$_2$ data set includes a new volcanic SO$_2$ flag aiming at discriminating pixels belonging to the SO$_2$ plume from other pixels and, in a first step, we wish to evaluate this flag. Figure 18 shows an example of maps for the 23rd August 2008 of the GOME-2A SO$_2$ columns, with no filtering (upper panel), applying the SO2_Volcano_Flag (center panel) and filtering all pixels with SO$_2$ column lower than a certain threshold (bottom panel). For the latter data selection, we have taken (for this particular case) a cutoff value of 0.75 DU which appears to be a good compromise to separate the pixels with elevated volcanic SO$_2$ from those that are mostly affected by noise. From Fig 14, one can see that the SO2_Volcano_Flag is able to detect volcanic plumes but it misses a significant part of the SO$_2$ emitted (filamentary plumes). This is to be expected because the algorithm used to generate the SO2_Volcano_Flag was initially developed to notify the users of the SACS system on new volcanic activity and is rather conservative (see Brenot et al., 2014). Although the SO2_Volcano_Flag appears to form a useful information tool for several users of the GOME-2 SO$_2$ products (e.g., MACC; https://www.gmes-atmosphere.eu/) we recommend to further develop and refine this flag. One option would be to use a latitudinal-dependent threshold on the (background corrected) SO$_2$ slant columns corresponding to the detection limit at the 3σ value level (or more). The latter threshold would then be regularly updated to account for the possible instrumental degradation affecting the noise level.

We now compare the total SO$_2$ masses retrieved by GOME-2 and OMI for the eruption of Kasatochi. Figure 19 shows the SO$_2$ time series for the 7-31 August 2008 time period as well as the ratio between the GOME-2 and OMI SO$_2$ masses estimates.
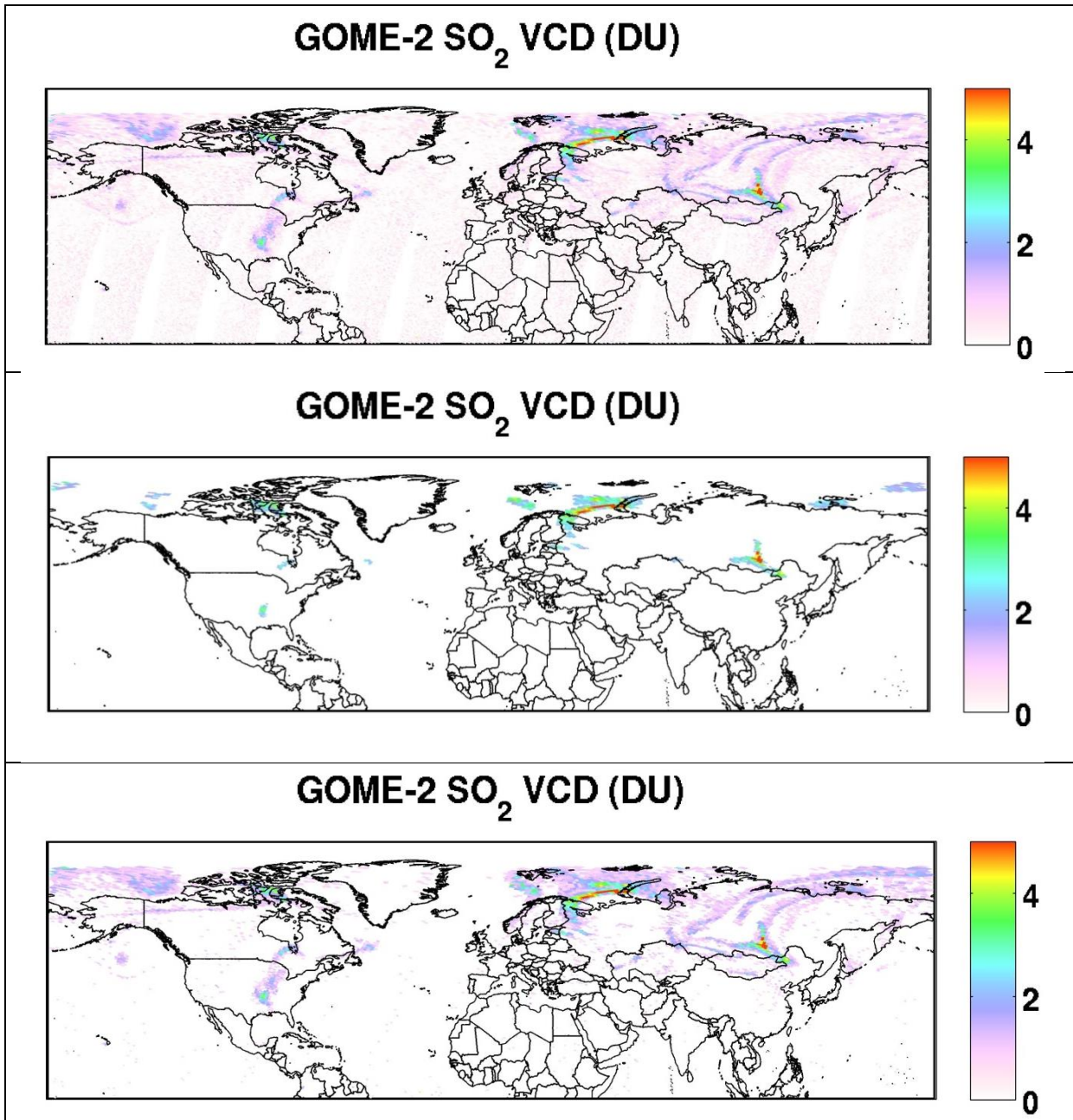
Figure 18: Sulfur dioxide vertical columns from GOME-2 measurements on August 23, 2008, for all pixels (upper panel), applying the SO2_Volcano_Flag (center panel), selecting the pixels with SO₂ VCD>0.75 DU (lower panel).
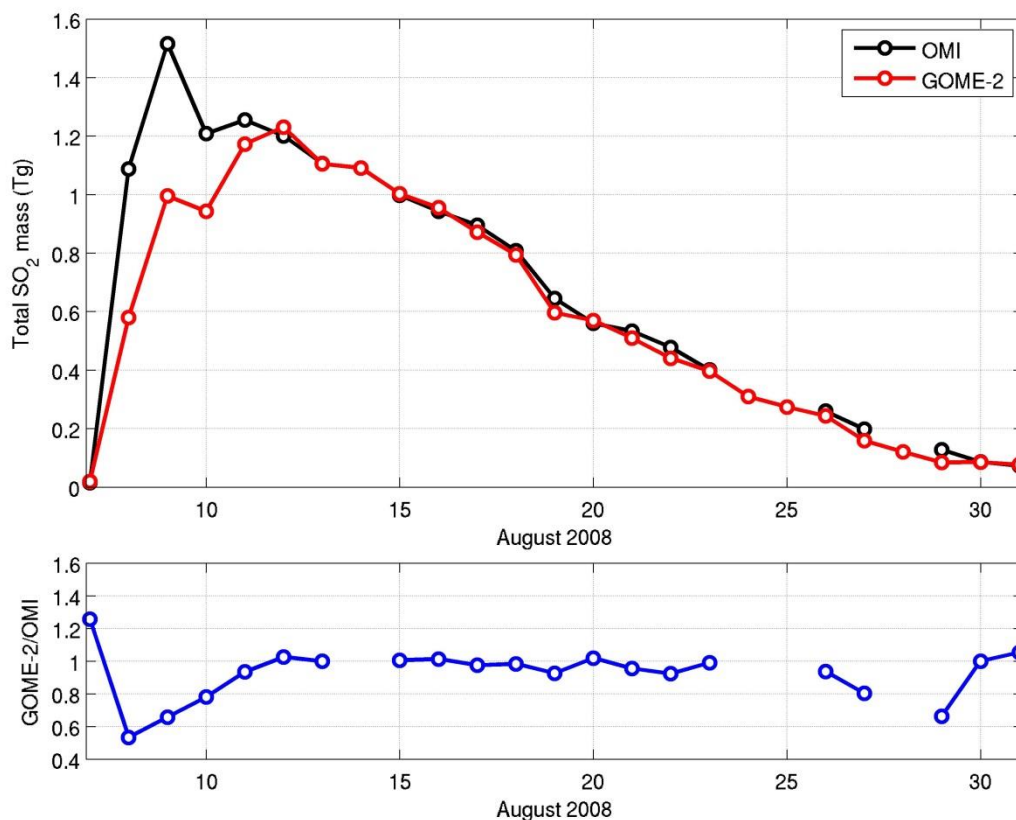
Figure 19: (upper panel) Total SO$_2$ masses measured by OMI and GOME-2 after the eruption of Kasatochi in August 2008, (lower panel) corresponding ratio of GOME-2 divided by OMI total SO$_2$ masses.

At the beginning of the eruption (8-10 August), it is clear that GOME-2 underestimates the SO$_2$ mass retrieved by OMI up to a factor of 2. On 8 August 2008, the maximum SO$_2$ VCD measured by GOME-2 is of 140 DU, compared to 382 DU from OMI. This underestimation is due to (well known) non-linear/saturation effects at high SO$_2$ VCD in the 312-326 nm wavelength range of GOME-2. This is not the case for OMI because other fitting windows (325-335 nm and 360-390 nm) are used to avoid this saturation issue. From 11 August onwards, GOME-2 is in close agreement with OMI (differences mostly within 20%). It should be noted however that the total SO$_2$ masses at the tail of the curves are significantly depending on the pixels selection criteria, both for GOME-2 (VCD>0.75 DU) and OMI (VCD>0.5 DU) data sets. Having said that, this Figure nicely demonstrates the usefulness of the GOME-2 SO$_2$ dataset to monitor volcanic SO$_2$ loadings.

As a second case study, Figure 20 shows a comparison between the total SO$_2$ mass time series of GOME-2 and OMI for the eruption of Sarychev, Russia, in June 2009. For this case, the saturation issue of GOME-2 is less pronounced than for Kasatochi and happens only occasionally (e.g., 17 June). A striking feature of Figure 20 is that GOME-2 retrievals are higher than OMI at the beginning of the eruption (12-15 June 2009). This is related to the data filtering of OMI for the row anomaly which became stronger in 2009 compared to 2008 (Figure 19). Overall, one can conclude from Figure 19 that OMI and GOME-2 agree fairly well (e.g., within 20% for 20-30 June), in line with Figure 19.
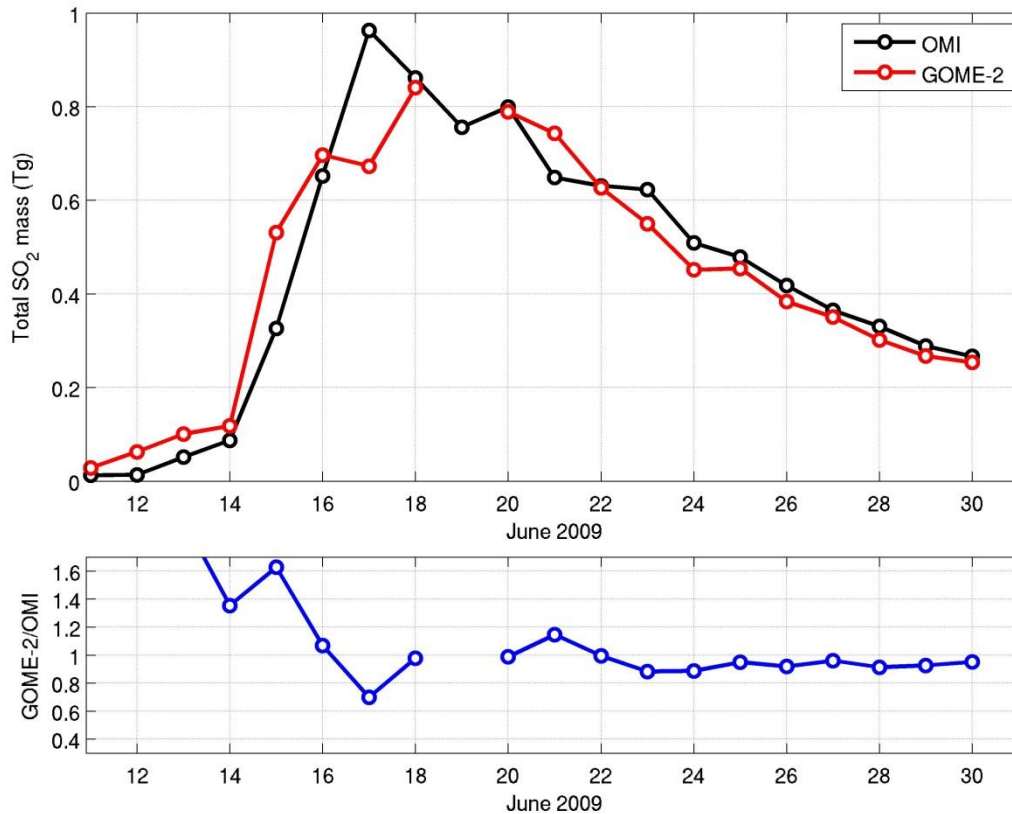
Figure 20: (upper panel) Total SO_2 masses measured by OMI and GOME-2 after the eruption of Sarychev in June 2009, (lower panel) corresponding ratio of GOME-2 divided by OMI total SO_2 masses.

From Figure 19 and 17, one can conclude that the GOME-2A SO_2 column product nicely captures the SO_2 plumes and provides reasonable quantitative values for the total SO_2 masses, except for (rare) cases with extreme SO_2 loadings.

As a last example, we wish to compare the SO_2 columns measured by GOME-2A and GOME-2B and check for consistency. For the period when both GOME-2A and GOME-2B operated in their nominal mode (from December 2012 until July 2013), there was one large eruption (Copahue, Chile) in the end of December. Figure 21, shows examples of SO_2 maps from GOME-2A and GOME-2B for the 24th December. It is clear that, overall, both instruments succeeded in detection the SO_2 plume and the measured SO_2 columns are similar, although GOME-2A has a tendency to give slightly higher values than GOME-2B. Note that this case was already investigated in a previous report for the GDP4.7 version (Theys et al., 2013) and basically the same conclusions apply for the version GDP4.8.
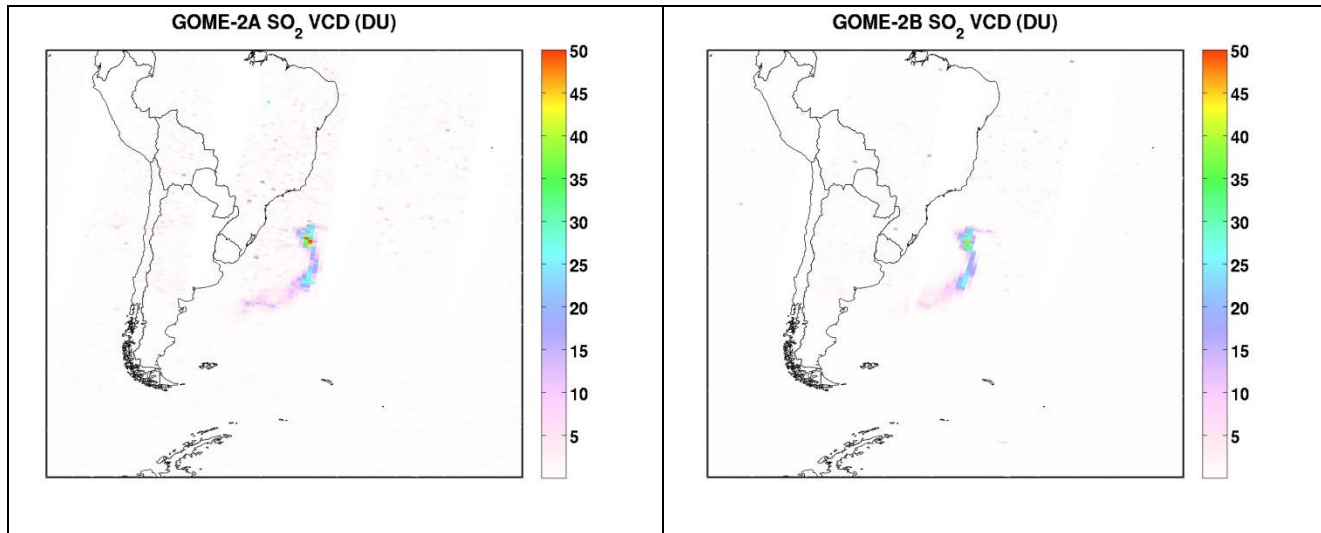
Figure 21: Example of SO$_2$ vertical columns for the December 24, 2012, as measured by GOME-2A (left) and GOME-2B (right).

C.2.2 Investigating the case for anthropogenic SO$_2$

As a first step, we evaluate the new data set for its ability to detect the large anthropogenic emissions sources using global yearly SO$_2$ maps of background corrected slant columns. Figure 22 shows examples for GOME-2A in 2007 (beginning of operations) and both GOME-2A and GOME–2B for 2013. For these maps, no cloud filtering was applied. Only the pixels selection criteria on SZA, viewing mode, flag and index in scan have been used.

GOME-2A SO$_2$ SCD (DU) - 2007


GOME-2A SO$_2$ SCD (DU) - 2013
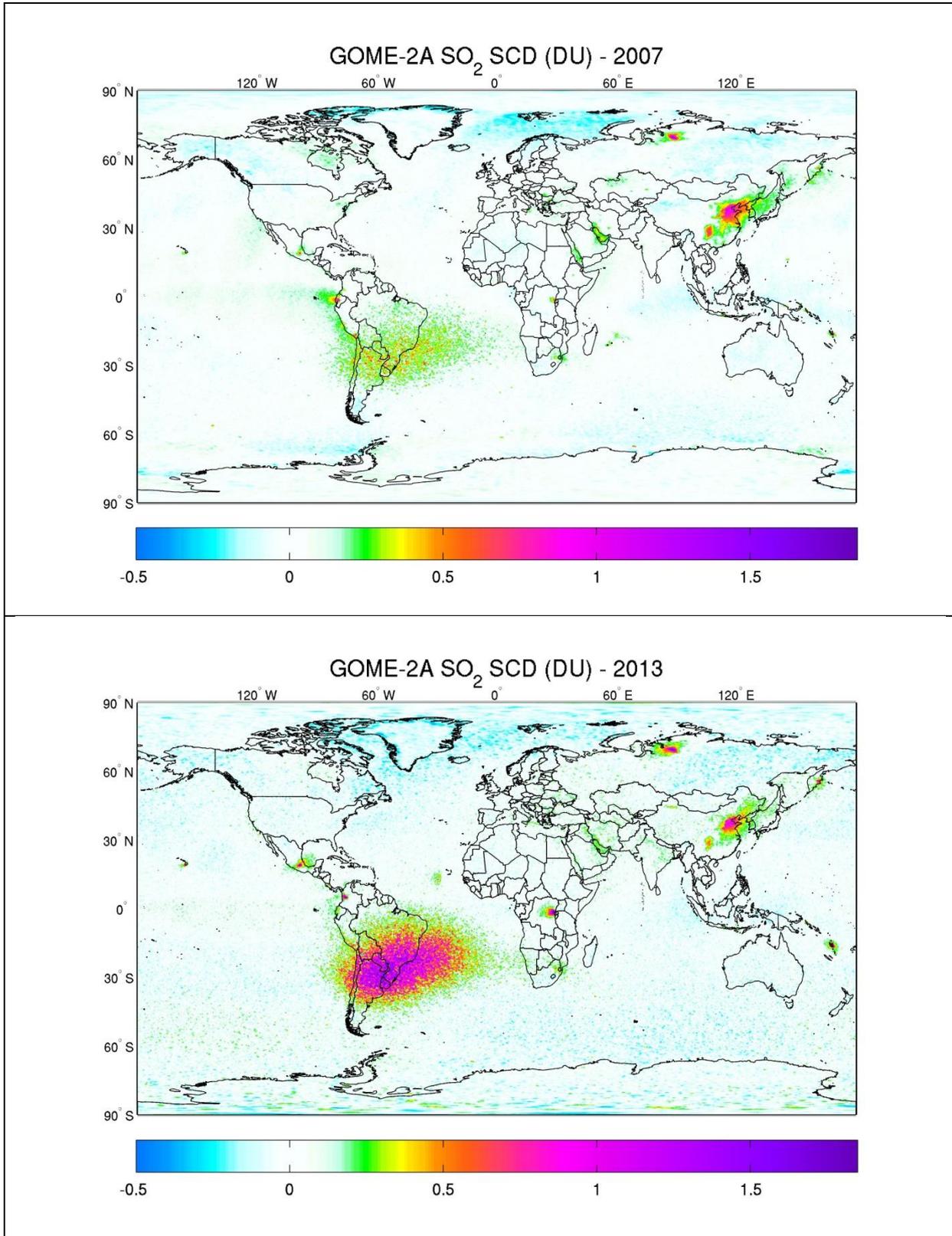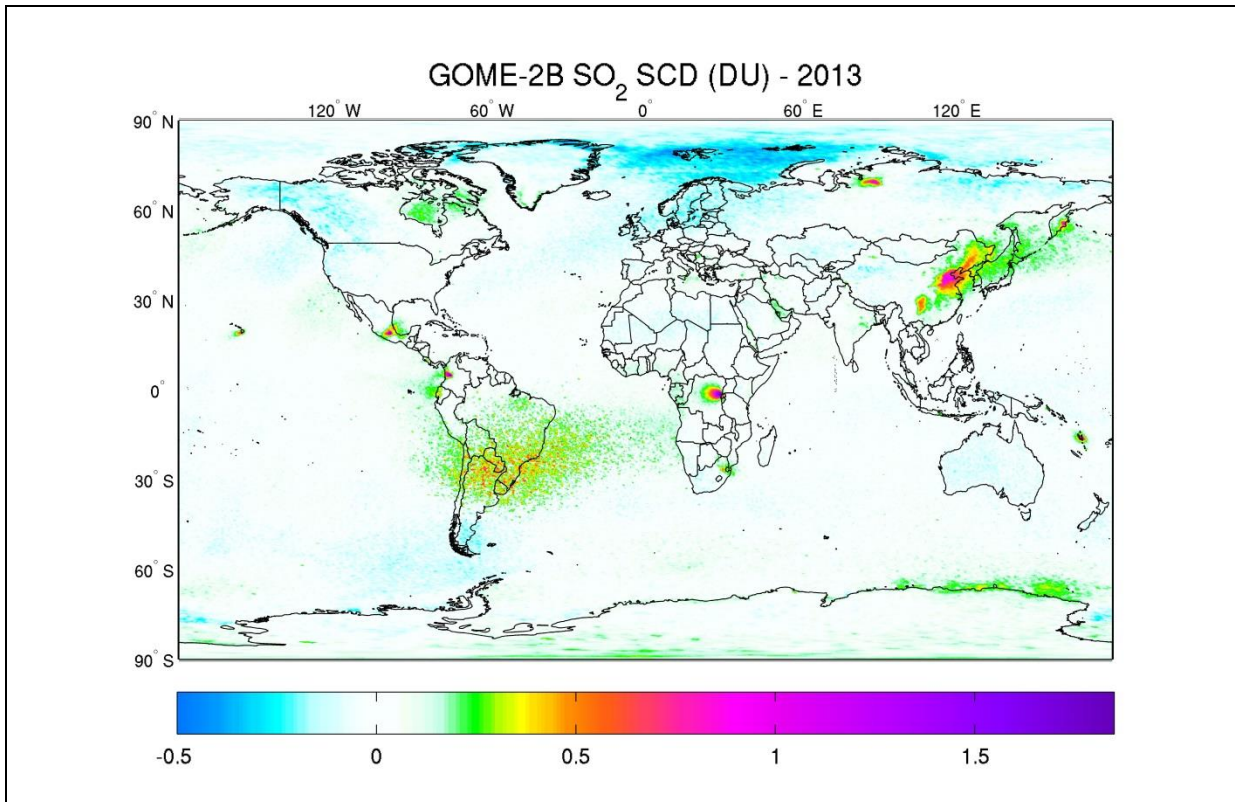
Figure 22: Yearly averaged SO_2 slant columns averaged background from GOME-2A (top panel: 2007, middle panel: 2013) and GOME-2B (lower panel: 2013). Only data corresponding to solar zenith angles lower than 70° are shown. Note that the color scale of the column maps has been chosen in a way that all features (including negative columns) can be best visualized.

Several remarks can be made, mostly in line with the results of Section C1:

1. A number of emission hotspots can be identified, in agreement with previous work of Fioletov et al. (2013). In addition to some well-known degassing volcanoes, an SO_2 signal from pollution is clearly detected over China, Norilsk, South Africa, Eastern Europe and US (in 2007 only) and Middle East (oil industry).

2. Several artifacts are also apparent in Figure 22:
   a. At high latitudes, a general tendency to produce negative columns is observed for GOME-2A. This problem is even more pronounced for GOME-2B at Northern high latitudes while positive SO_2 columns can be seen in the Antarctic region (notably for coastal areas). We note however most of the available SO_2 products have limitations at high latitudes (Fioletov et al., 2013). A striking feature as well is found over the Hudson Bay where elevated values of SO_2 are found in both GOME-2A and –B datasets. The reason for this artifact is unknown but might be related to a weather pattern there leading to lower tropopauses (hence higher O_3 columns).
   b. Both GOME-2A and –B SO_2 column products are very sensitive to the South Atlantic Anomaly, SAA and for that reason we recommend the application of a spike removal correction, see Richter et al., 2011. For 2013, one can see that GOME-2A is dramatically affected by this issue. The reason for this is related to the use of the inverse of the Earthshine radiance in the intensity offset correction (see discussion in Section C1).

   It is also clear from Figure 22 (middle panel) that the background SO_2 levels outside the SAA region are generally negative and it is unclear why that is the case.

Figure 23 shows another example of comparison between results from GOME-2A and OMI (Theys et al., 2015) for the year 2007 over China. To produce these SO_2 maps, clear-sky pixels with cloud fractions less than 30% have been selected and a fixed AMF of 0.4 (typical for a boundary layer SO_2 profile) has been applied to the background corrected slant columns, both for GOME-2 and OMI.
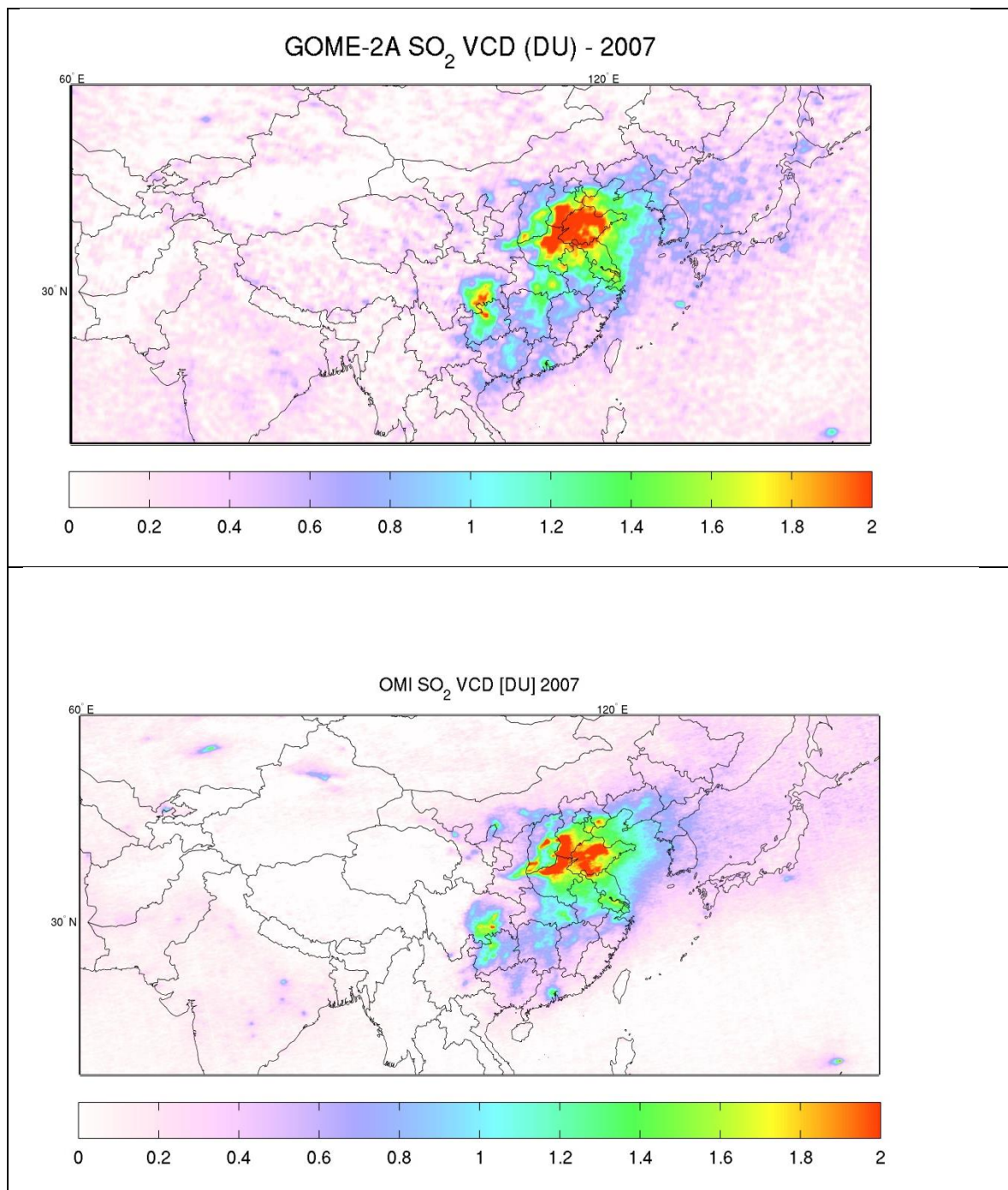

Figure 23: SO_2 vertical columns (DU) averaged for 2007 for clear-sky pixels (cloud fraction less than 0.3) for the GOME-2A (top panel) and OMI (bottom panel) instruments.

Although the GOME-2 data are more noisy than OMI and some emissions spots are not detected by GOME-2, one can see that, at first glance, similar patterns are observed by both sensors in Eastern China and that the absolute values are comparable, with GOME-2 having a general tendency to produce higher values.

C.2.2.1 Comparison with MAX-DOAS measurements at Xianghe

The multi-axis DOAS instrument at Xianghe is a system developed by BIRA-IASB, and operated by the Institute of Atmospheric Physics (IAP), Chinese Academy of Sciences. The description of the retrieval technique and presentation of the results, including validation against in-situ measurements, can be found in Wang et al. (2014). The SO_2 profiles data set covers the period March 2010 until December 2013 and has been used in Theys et al. (2015) to validate BIRA-IASB OMI SO_2 columns.

Here we aim at validating the GOME-2 SO_2 columns for the new GDP4.8 profile called *1km* (which is also used for the NASA OMI SO_2 operational product (Li et al., 2013)), representing the scenario of anthropogenic SO_2 emissions (Taubmann et al., 2006).

The comparison between the ground-based and GOME-2 SO_2 columns is done as follows: first, all GOME-2 (A and B separately) clear-sky pixels (i.e., cloud fractions less than 0.3) within a 150 km circle radius around Xianghe and surface height less than 500 m (to exclude observations over clean elevated regions) with solar zenith angles less than 70° are selected (in addition to the recommended pixel selection criteria, like viewing mode, index in scan, etc.). Then, for each pixel, all MAX-DOAS data within ± 90 minutes of the GOME-2 overpass time are considered and averaged for the comparison. In contrast to the OMI validation, we have not corrected the GOME-2 SO_2 columns using the MAX-DOAS mean SO_2 profile. Doing so would allow (in principle) a consistent comparison between MAX-DOAS and GOME-2 SO_2 VCDs, but unfortunately the information on averaging kernels (needed for this step) is not provided in the GOME-2 L2 files. We have not attempted to recalculate AMFs using the BIRA-IASB tools because there are probably differences with the approach and settings used in the operational processing environment.

Figure 24 shows the comparison between the monthly averaged ground-based (black dots) and coincident GOME-2A SO_2 columns for the period 03.2010-12.2013, at Xianghe.

We have considered both SO_2 vertical columns using total AMFs (cyan) and clear-sky AMFs (red).

One can see that generally the MAX-DOAS and GOME-2 columns agree reasonably well and the seasonal cycle of SO_2 is consistent in both datasets. Among the two GOME-2 estimations, the results using the clear-sky AMFs are in a better agreement with the MAXDOAS values than the retrievals based on total AMFs. We note also that the cloud corrected values (using total AMFs) are always lower than the uncorrected ones and the reason for this is because of the absence of a "ghost" (below cloud) column correction. One can argue whether a cloud correction should be applied or not (given the uncertainties on cloud retrievals and a-priori profiles) but if it is the case then a ghost correction should be included (as it is the case for other GOME-2 trace gas products, such as NO_2 and HCHO). In Figure 24 bottom panel, the differences between GOME-2A (clear-sky) and MAX-DOAS columns are shown. As discussed before the agreement is reasonably good especially for non-winter periods and the product reaches often the target/optimal accuracy (50%/30%) and the threshold accuracy (100%) otherwise. Nevertheless, from Figure 24, it is not possible to really consolidate these results because only one a-priori profile has been used for GOME-2 AMF calculation for the whole time series, which is arguably a crude assumption.

A striking feature in Figure 24 is also a general positive trend in the differences (GOME-2A vs MAXDOAS) and the reason for this anomaly will be investigated in the next section.

We have estimated the relevant statistical parameters of the bi-variate linear regression GOME-2A clear-sky columns versus MAX-DOAS (the scatter plot is shown on Figure 25). The correlation coefficient is equal to 0.64 and the slope of the linear regression fit is 1.23.
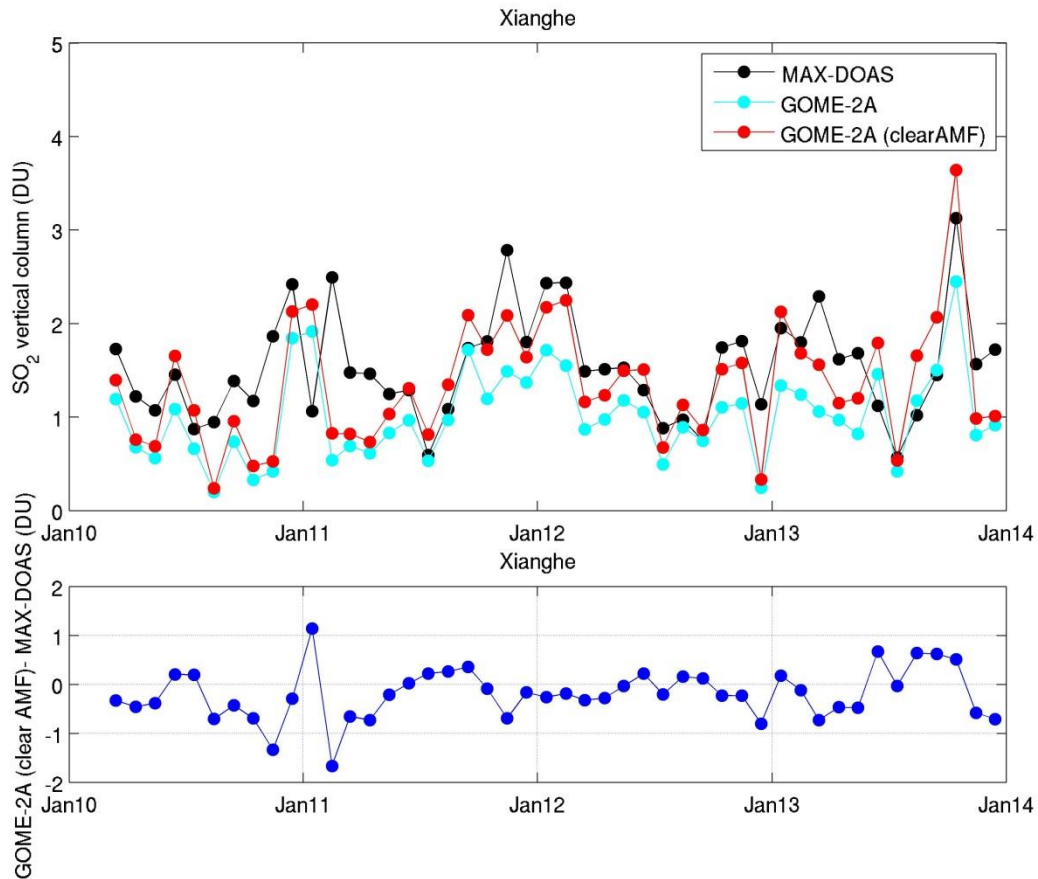

Figure 24: (top) Comparison of monthly averaged SO_2 columns at Xianghe for the period 2010-2013 measured by the MAX-DOAS and GOME-2A (using the anthropogenic SO_2 emissions profile). Two assumptions are made for the GOME-2 AMFs: total AMFs (in cyan) and clear-sky AMFs (in red), (bottom) Time series of the SO_2 column differences between GOME-2A (using clear-sky AMFs) and MAXDOAS.
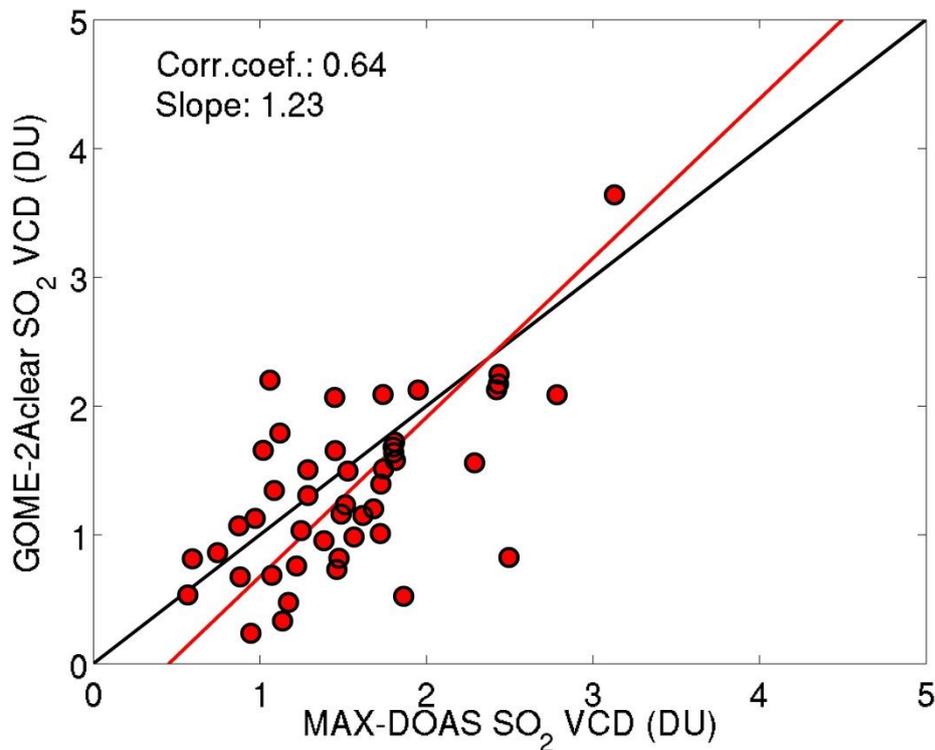
Figure 25: Scatter plot of GOME-2A SO$_2$ columns (calculated using clear-sky AMFs) versus MAX-DOAS SO$_2$ columns. Statistical parameters (correlation coefficient and slope of the linear regression (red line)) are given inset. The black line is the 1:1 line.

Figure 26 and 24 are the equivalent comparison results for GOME-2B for the year 2013. Generally the same findings as for GOME-2A also apply for GOME-2B: (a) SO$_2$ columns using clear-sky AMFs are larger than for total AMFs and are in a better agreement with the MAX-DOAS retrievals, (b) the GOME-2B (clear-sky) SO$_2$ columns are close to the MAXDOAS values except for winter. From Figure 27, the correlation coefficient is equal to 0.55 and the slope of the linear regression (GOME-2B clear-sky columns versus MAX-DOAS) fit is 1.49. However, we should be noted that these statistical parameters are significantly influenced by two outlier points.
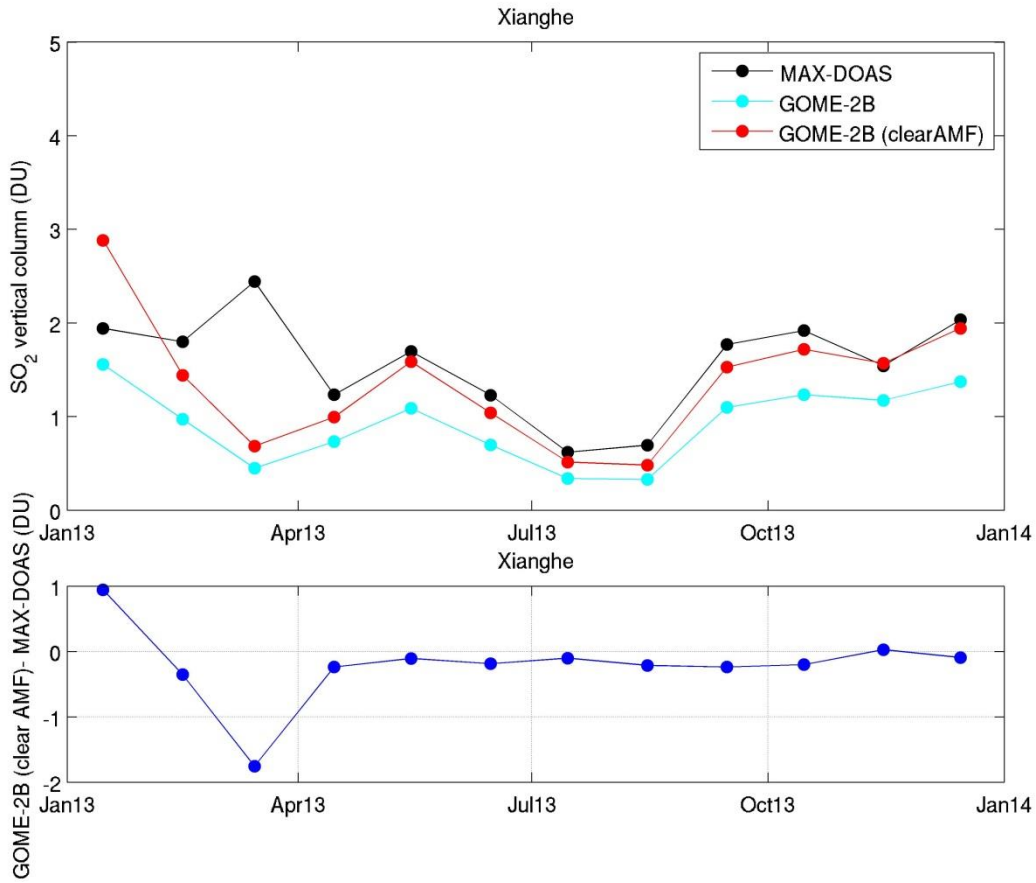
Figure 26: (top) Comparison of monthly averaged SO$_2$ columns at Xianghe for the year 2013 measured by the MAX-DOAS and GOME-2B (using the anthropogenic SO$_2$ emissions profile). Two assumptions are made for the GOME-2 AMFs: total AMFs (in cyan) and clear-sky AMFs (in red), (bottom) Time series of the SO$_2$ column differences between GOME-2B (using clear-sky AMFs) and MAXDOAS.
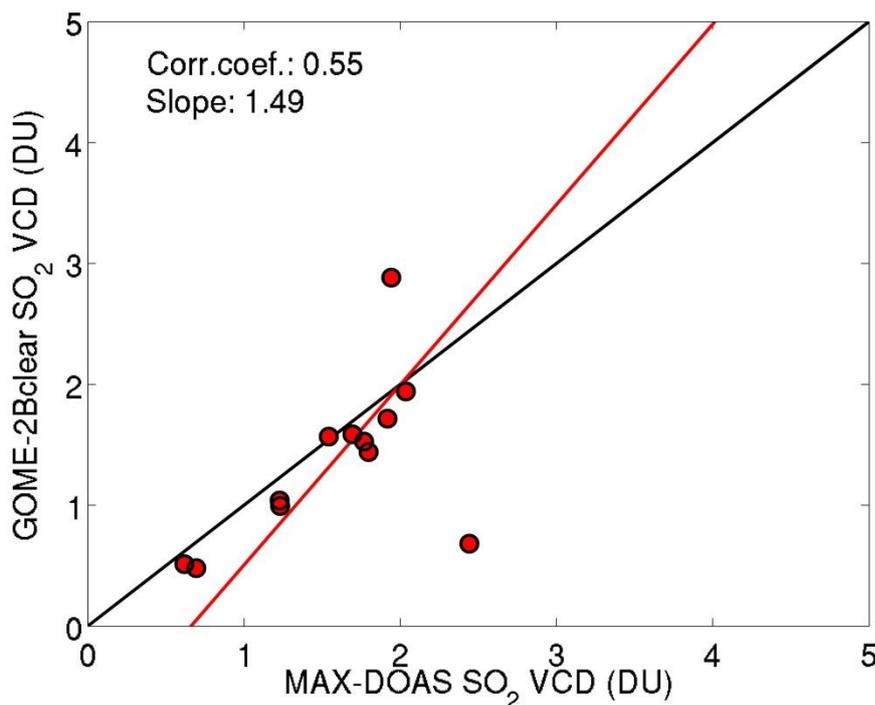

Figure 27: Scatter plot of GOME-2B SO$_2$ columns (calculated using clear-sky AMFs) versus MAX-DOAS SO$_2$ columns. Statistical parameters (correlation coefficient and slope of the linear regression (red line)) are given inset. The black line is the 1:1 line.

C.2.2.2 Stability of the GOME-2A and –B SO$_2$ column products as a function of time

Figure 28 shows time-series of SO$_2$ SCDs over the Equatorial Pacific averaged on a monthly basis for the GOME-2A and GOME-2B periods, and for different ranges of Line-of-Sight (LOS) angles (LOS<20°, 20°<=LOS<40°, LOS>=40°).

For GOME-2A, one can see that the SCD values are rather small at the beginning of the mission and then rapidly increase until beginning of 2009 when a strong decrease of the SCDs occurs. After the GOME-2A throughput test, the SCD values for the different LOS start to deviate significantly from each other, with absolute differences between low and high viewing angles up to 0.25 DU. We also notice an important negative trend in the SCDs from 2011 onwards. After July 2013, GOME-2A is in its reduced swath mode (hence no high LOS data) and the SCDs for low and medium LOS come closer to zero.

We interpret the behavior depicted in Figure 28 (top panel) as related to the time evolution of the shape of the instrumental slit function in the wavelength range used to retrieve SO$_2$. The actual slit function shape deviates quite quickly and significantly from the slit function characterized before the launch (and used in the DOAS fit of SO$_2$). A plausible impact on the spectral fitting is a reinforcement of the interference with ozone and this probably explains the erratic LOS dependence of the SCDs (the background correction

applied to the retrieved SCDs do not account for dependences neither on LOS nor on ozone absorption). Note that this effect is not limited to SO_2, and e.g. De Smedt et al. (2012) studied the impact of slit function changes on GOME-2 HCHO retrievals and implemented an improved procedure consisting in fitting asymmetric slit function parameters as part of the HCHO DOAS inversion.

For SO_2, several tests have been done as well and the BIRA-IASB Scientific GOME-2 SO_2 algorithm currently uses the shape of the slit function characterized before launch but allows for shift and stretch of the slit function during the DOAS process. Moreover, a background correction depending on LOS and measured ozone slant column is also applied. For the sake of completeness, we show in Figure 29 the results of the BIRA-IASB GOME-2A SO_2 product (but limited to the year 2010) and one can see that the problem in Figure 28 (top panel) is largely resolved.
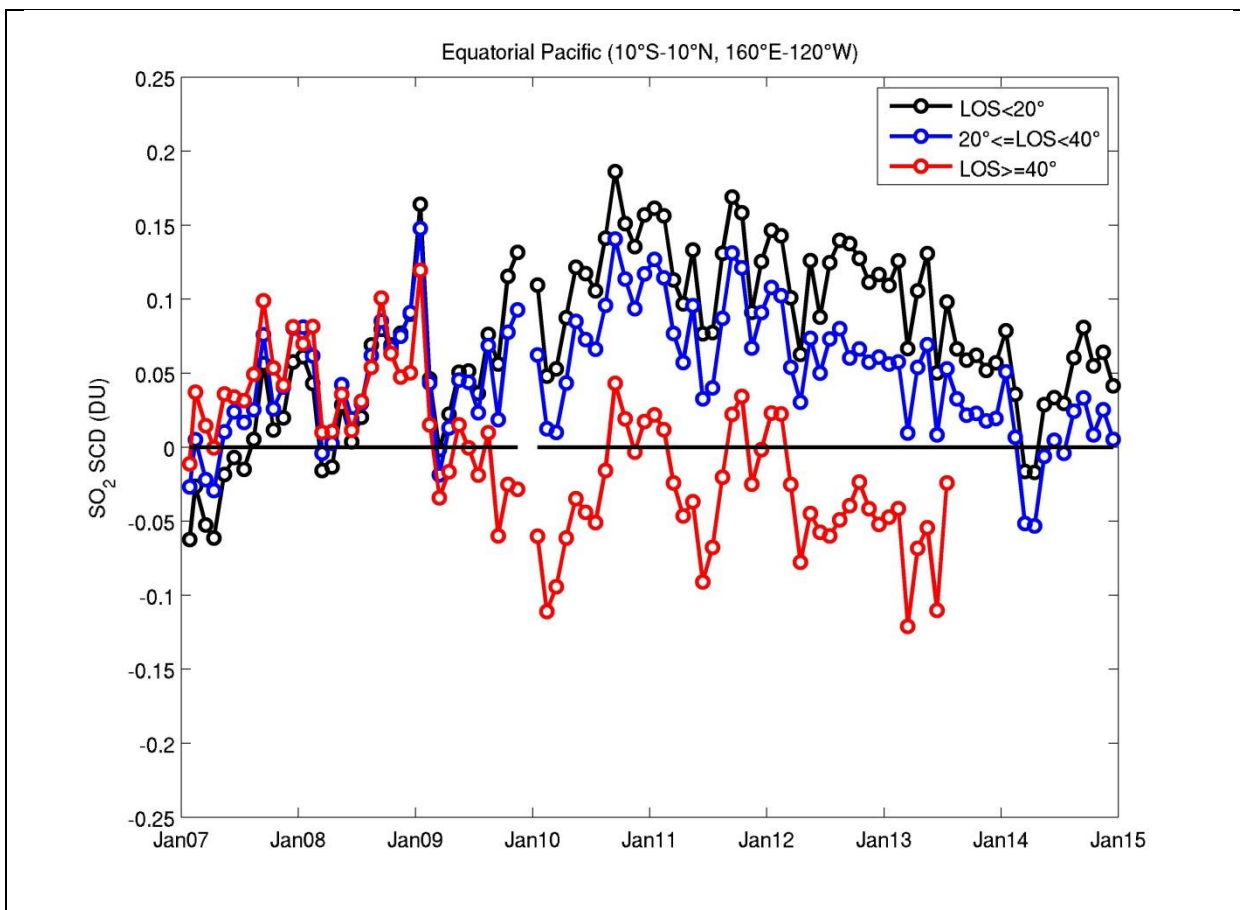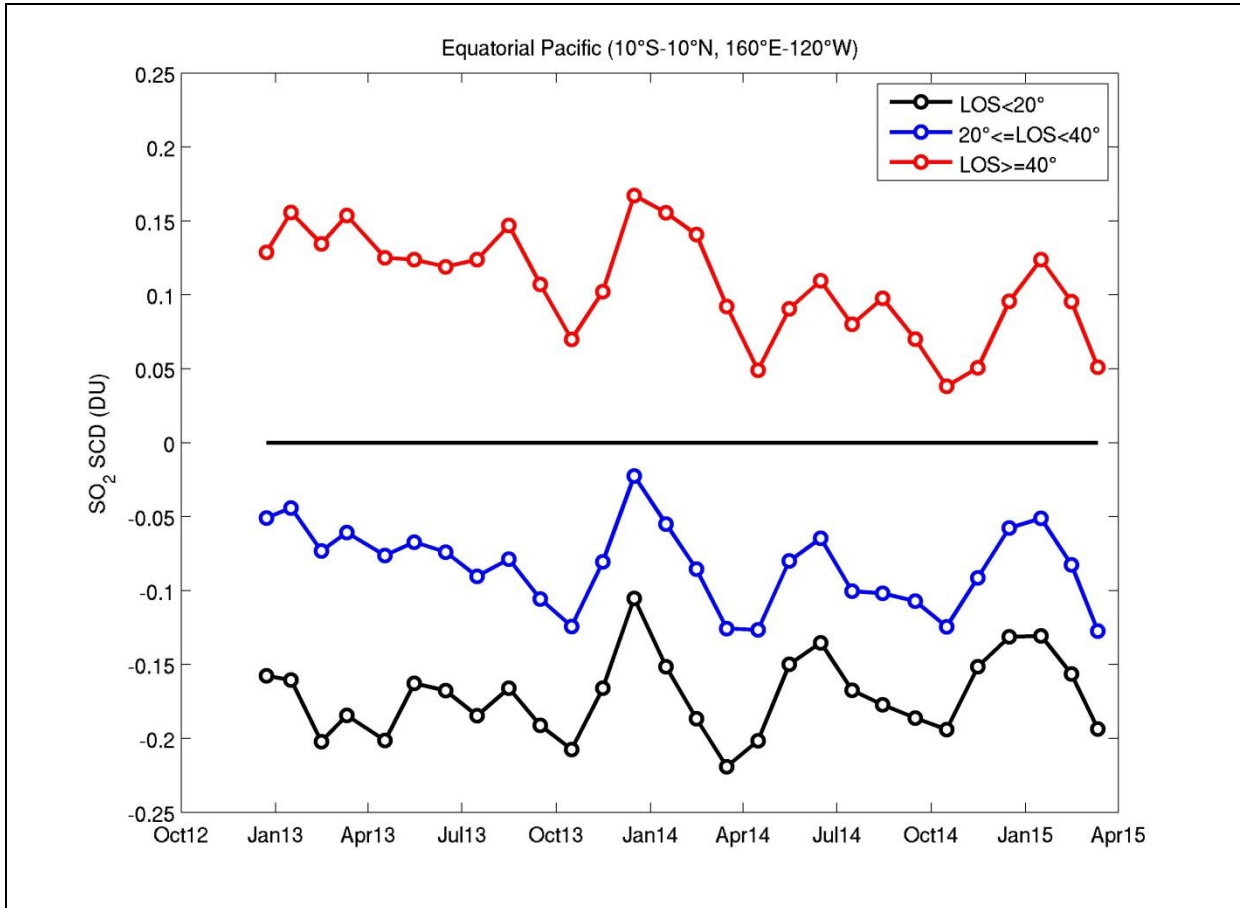
Figure 28: Time-series of monthly averaged SO₂ background corrected slant columns over the Equatorial pacific (10°S-10°N, 160°E-120°W) for different ranges of line-of-sight angles, for GOME-2A (upper panel) and GOME-2B (lower panel).
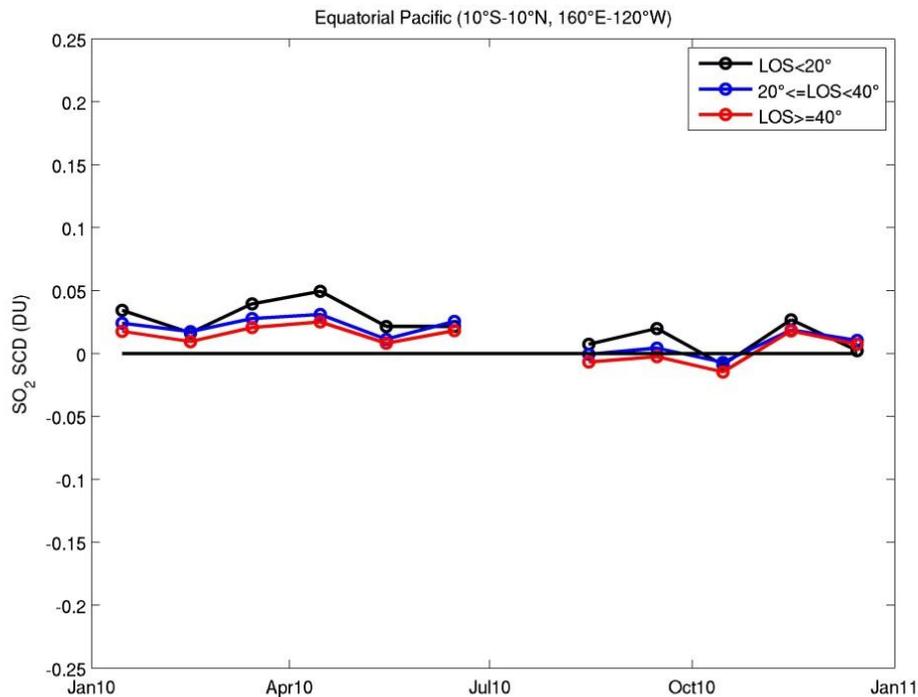
Figure 29: same as Figure 28 (upper panel) for the BIRA-IASB GOME-2A SO$_2$ product for the year 2010.

For GOME-2B, the results of Figure 28 (bottom panel) reveal a very strong LOS dependence of the SO$_2$ SCDs but relatively stable over time. This suggests an alteration of the slit function shape (relative to pre-launch slit function) already from the very start of the GOME-2B operations.

The same investigations have been performed at other places and Figure 30 shows, as an example, the results for Xianghe. Note that for the GOME-2A data (Figure 30, upper panel), only yearly averages are displayed (rather than monthly averages as in Figure 28), because the corresponding graph with monthly averaged values was found difficult to read (because of strong SO$_2$ variability at Xianghe), but it is does not change the overall conclusion.
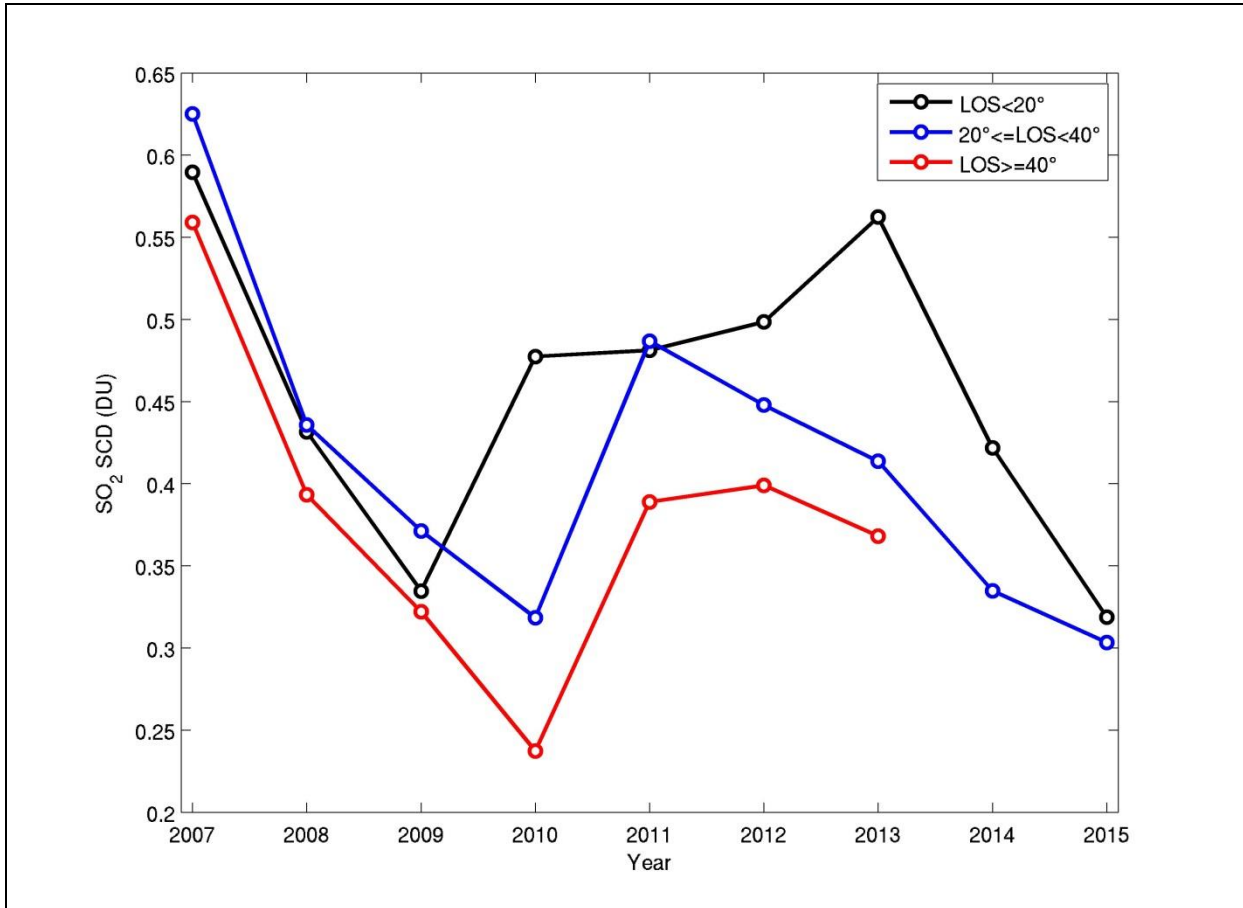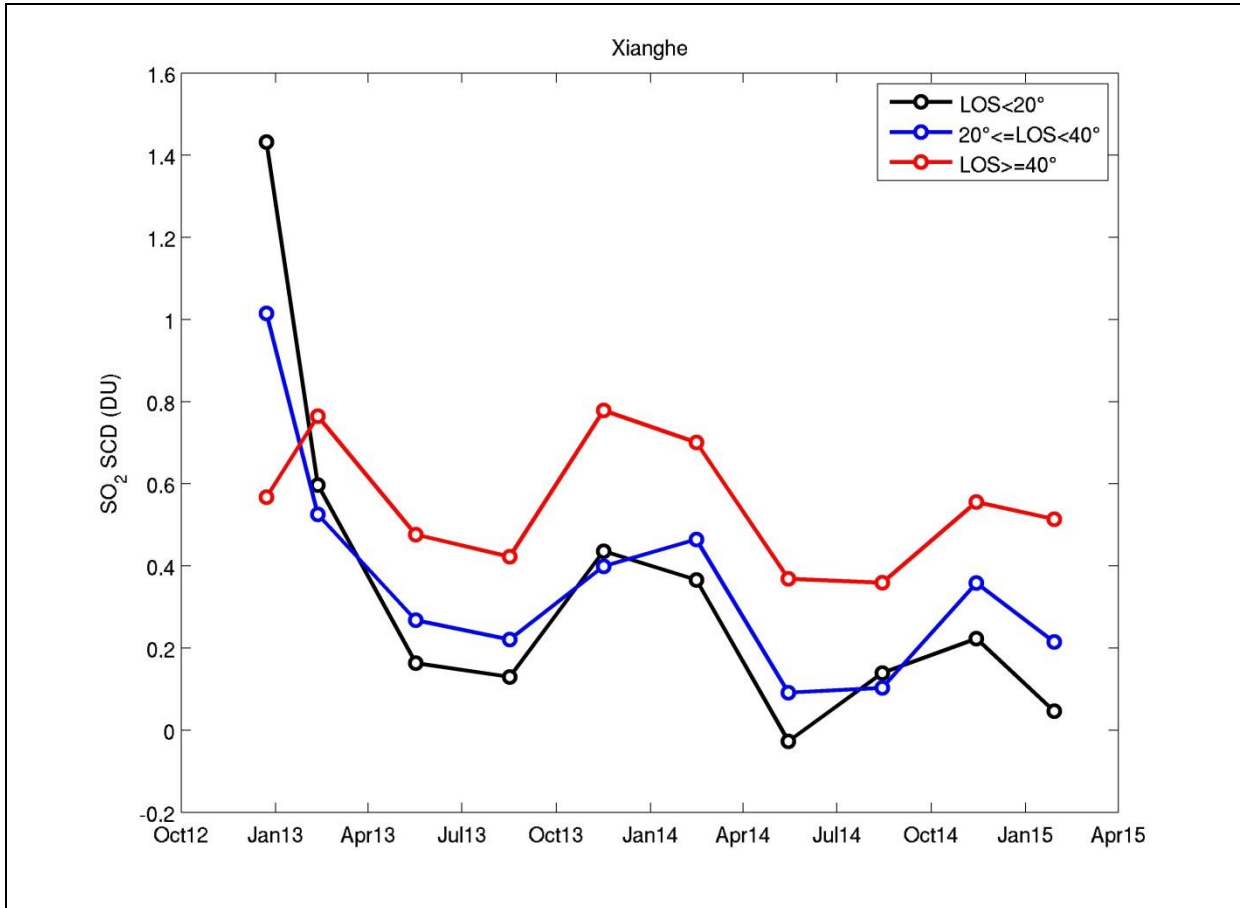
Figure 30: same as Figure 28, for the pixels within a 150 km circle radius around Xianghe. (top panel) GOME-2A yearly SO$_2$ SCD averages, (bottom panel) GOME-2B monthly SO$_2$ SCD averages.

It is obvious from Figure 30 that the LOS dependence over the Equatorial Pacific (Figure 28) is also clearly seen over Xianghe (both for GOME-2A and –B). If one consider the year 2010 (GOME-2A) for instance, the absolute difference in slant columns between the low and high LOS is up to ~0.25 DU. If ones assumes a typical AMF of 0.45-0.5 for a polluted scene (see Figure 13 of the SO$_2$ ATBD; Valks et al., 2015), this translates into an error on the SO$_2$ vertical columns of 0.5-0.55 DU (and more in winter). For GOME-2B, this effect is even larger (the corresponding error on the vertical columns is easily higher than 1 DU). We recommend to further work on this issue to gain confidence in the data and its evolution with time.

D.   CONCLUSIONS

This document reports on the validation of NRT, offline and reprocessed GOME-2A and -B SO_2 column data products retrieved at DLR with versions 4.8 of the GOME Data Processor (GDP), using level-1B data based on the level-0-1B processor version 5.x and 6.0.

Compared to the previous data version, the new GDP4.8 SO_2 product has three new important and notable features: (a) consistent retrieval settings have been applied to both GOME-2A and GOME-2B sensors, (b) a boundary layer SO_2 product, similar to the PBL OMI/Aura product, has been introduced and (c) a volcanic flag has been implemented.

GOME-2A & B SO_2 vertical columns have been evaluated using (1) comparisons with previous version (4.7) of the algorithm and by assessing the consistency between the two sensors (for GDP4.8 version), (2) comparisons with correlative data sets from OMI (PCA and DOAS algorithms) and MAX-DOAS measurements at Xianghe, China.

Note that the conclusions are based on the original GDP4.8 dataset made available to the validation team in late May 2015. Following the first results of the validation process which were made available to the operational team, a suite of new GDP4.8 algorithm test runs were performed for years 2008 and 2013 that could solve some of the issues identified hereafter.

The following main conclusions can be drawn:

- ▪ Comparison of GDP4.7 and GDP4.8: For the slant columns, there are negligible differences between the two versions for GOME-2B while for GOME-2A the slant columns show some differences. An important feature in GOME-2A is a stronger effect of the South Atlantic Anomaly (see below). For the vertical columns, the data are found to be noisier in the new version and the GOME-2A GDP4.8 2.5km plume height product shows between 0 and 0.5-1 D.U. higher SO2 loading on a yearly basis than the GDP4.7 algorithm, whereas for GOME-2B this increase is smaller, between 0 and 0.5 D.U. at the known hot spots. Retrievals tests have shown that this was due to the use of the inverse of the Earthshine spectrum in the DOAS intensity offset correction; this issue is largely solved by using instead the inverse of the Solar spectrum. This setting is the new baseline for the GDP4.8 SO_2 algorithm.

- • GOME-2A- GOME-2B-OMI consistency: 33 known SO_2 emitting locations around the world, including volcanoes, power plants, smelters, and so on, were used to compare the GOME-2A and -2B SO_2 to the OMI estimates. The average SO_2 loading of these sources was 0.41±0.31 D.U. for GOME-2A, 0.08±0.24 D.U. for GOME-2B and 0.30±0.31 D.U. for OMI. GOME-2A was found to be in better agreement with OMI than GOME-2B GDP4.8 due to the higher amount of negative mean loadings shown by the newer instrument. However, the mean correlation coefficient for these sites between GOME2 and OMI was found to be 0.42 for GOME-2A and 0.51 for GOME-2B pointing to the fact that both GOME-2A and –2B GDP 4.8 SO_2 column retrievals fare well with OMI/Aura considering all the limitations.

- • Volcanic SO_2: GOME-2A and –B GDP 4.8 SO_2 column retrievals is clearly able to capture and track plumes after small to strong eruptions, but the newly implemented flag for volcanic SO_2 misses parts of aged and filamentary plumes. Quantitatively, the SO_2 masses estimated from GOME-2 after strong eruptions agree very well with OMI (with differences mostly within the 30% optimal accuracy), except for the rather unusual very high SO_2 amounts (for the first days after the start of the eruption) where GOME-2 underestimates the columns (saturation effect).

- Anthropogenic SO_2: the addition of a new SO_2 column in GDP4.8 using a typical profile for anthropogenic emissions scenario is an improvement and allows direct comparison with OMI. From comparisons with OMI, it can be concluded that 1) several hotspots are seen by both satellite datasets and the mean values from GOME-2 and OMI are reasonably close, 2) some weak emissions are not detected by GOME-2, partly because of the better spatial resolution of OMI but also because GOME-2 data is more noisy. From the comparison (using the anthropogenic SO_2 column field) with the MAXDOAS-data, the best agreement is found for the results using clear-sky AMFs (while the results for total AMFs are always found lower). The agreement is reasonably good especially for non-winter periods and the product reaches often the target/optimal accuracy (50%/30%) and the threshold accuracy (100%) otherwise.

- Localized artefacts and product self-inconsistency: Several artefacts are found in the maps e.g. at high latitudes. Over the SAA region specifically, the GOME-2 data shows a dramatic trend over time with noisy and elevated SO_2 columns over the last years (this effect is worst in GDP4.8 than GDP4.7). This feature is due to the treatment of the DOAS intensity offset correction An investigation of the SO_2 SCDs over clean and polluted regions shows an anomalous dependence of the results with viewing angles for both sensors. The most likely explanation for this effect is due to differences between the slit functions used in the spectral fitting (extracted from the GOME-2 key data) and the actual ones.

E.   REFERENCES

E.1 Applicable documents

[ATBD]   Algorithm Theoretical Basis Document for GOME-2 Total Column Products of Ozone, NO_2, BrO, SO_2, H_2O, HCHO and Cloud Properties (GDP 4.8 for O3M-SAF OTO and NTO), DLR/GOME-2/ATBD/01, Rev. 3/A, Valks, P., et al., March 2015.

[PUM]   Product User Manual for GOME-2 Total Column Products of Ozone, NO_2, BrO, SO_2, H_2O, HCHO and Cloud Properties, DLR/GOME-2/PUM/01, Rev. 3/A, Valks, P., et. al., 2015.

[PRD]   Product Requirements Document, SAF/O3M/FMI/RQ/PRD/001/Rev. 1.7, D. Hovila, S. Hassinen, D. Loyola, P. Valks, J., S. Kiemle, O. Tuinder, H. Joench-Soerensen, F. Karcher, 2015.

E.2 Reference documents

E.2.1 Peer-reviewed articles

Bogumil, K., J. Orphal, T. Homann, S. Voigt, P. Spietz, O.C. Fleischmann, A. Vogel, M. Hartmann, H. Kromminga, H. Bovensmann, J. Frerick, J.P. Burrows (2003), Measurements of molecular absorption spectra with the SCIAMACHY pre-flight model: instrument characterization and reference data for atmospheric remote-sensing in the 230-2380nm region, Journal of Photochemistry and Photobiology, A:Chemistry, 157 , 167-184.

Brenot, H., Theys, N., Clarisse, L., van Geffen, J., van Gent, J., Van Roozendael, M., van der A, R., Hurtmans, D., Coheur, P.-F., Clerbaux, C., Valks, P., Hedelt, P., Prata, F., Rasson, O., Sievers, K., and Zehner, C.: Support to Aviation Control Service (SACS): an online service for near real-time satellite monitoring of volcanic plumes, Nat. Hazards Earth Syst. Sci., 14, 1099-1123, doi:10.5194/nhess-14-1099-2014, 2014.

Brion, J., et al.: Absorption spectra measurements for the ozone molecule in the 350-830 nm region, J. Atmos. Chem., 30, 291-299, 1998.

Carn, S. A., A. J. Krueger, N. A. Krotkov, K. Yang, and P. F. Levelt (2007a), Sulfur dioxide emissions from Peruvian copper smelters detected by the Ozone Monitoring Instrument, Geophys. Res. Lett., 34, L09801, doi:10.1029/2006GL029020.

Carn, S.A., N.A. Krotkov, K. Yang, R.M. Hoff, A.J. Prata, A.J. Krueger, S.C. Loughlin, and P.F. Levelt (2007b), Extended observations of volcanic SO_2 and sulfate aerosol in the stratosphere, *Atmos. Chem. Phys. Discuss.*, 7, 2857-2871. (http://www.atmos-chem-phys-discuss.net/7/2857/2007/acpd-7-2857-2007.html)

Carn, S.A., A.J. Krueger, N.A. Krotkov, S. Arellano, and K. Yang (2008a), Daily monitoring of Ecuadorian volcanic degassing from space, *J. Volcanol. Geotherm. Res.,* (in press).

Carn, S.A., A.J. Krueger, N.A. Krotkov, K. Yang, and K. Evans (2008b), Tracking volcanic sulfur dioxide clouds for aviation hazard mitigation. *Natural Hazards, Special Issue on Aviation Hazards from Volcanoes* (in press).

Clarisse, L., Hurtmans, D., Clerbaux, C., Hadji-Lazaro, J., Ngadi, Y., and Coheur, P.-F.: Retrieval of sulphur dioxide from the infrared atmospheric sounding interferometer (IASI), Atmos. Meas. Tech., 5, 581-594, 2012.

De Smedt, I., Van Roozendael, M., Stavrakou, T., Müller, J.-F., Lerot, C., Theys, N., Valks, P., Hao, N., and van der A, R.: Improved retrieval of global tropospheric formaldehyde columns from GOME-2/MetOp-A addressing noise reduction and instrumental degradation issues, Atmos. Meas. Tech., 5, 2933-2949, doi:10.5194/amt-5-2933-2012, 2012.

Fioletov, V. E., C. A. McLinden, N. Krotkov, K. Yang, D. G. Loyola, P. Valks, N. Theys, M. Van Roozendael, C. R. Nowlan, K. Chance, X. Liu, C. Lee, and R. V. Martin: Application of OMI, SCIAMACHY, and GOME-2 satellite SO2 retrievals for detection of large emission sources, J. Geophys. Res. Atmos., 118, 11,399–11,418, doi:10.1002/jgrd.50826, 2013.

Gür, B., P. Spietz, J. Orphal, and J. Burrows (2005), Absorption spectra measurements with the GOME-2 FMs using the IUP/IFE-UB's calibration apparatus for trace gas absorption spectroscopy CATGAS, final report, Inst. of Environ. Phys., Univ. of Bremen, Bremen, Germany.

Krotkov, N.A., B. McClure, R.R. Dickerson, S.A. Carn, C. Li, P.K. Bhartia, K. Yang, A.J. Krueger, Z. Li, P.F. Levelt, H. Chen, P. Wang and D. Lu, Validation of SO_2 retrievals from the Ozone Monitoring Instrument over NE China, J. Geophys. Res., 2008, 113, doi:10.1029/2007JD008818.

Krotkov, N.A., S.A. Carn, A.J. Krueger, P.K. Bhartia, and K. Yang (2006). Band residual difference algorithm for retrieval of SO2 from the Aura Ozone Monitoring Instrument (OMI). *IEEE Trans.Geosci. Remote Sensing*, *AURA special issue*, 44(5), 1259-1266, doi:10.1109/TGRS.2005.861932, 2006

Krueger, A.J., L.S. Walter, P.K. Bhartia, C.C. Schnetzler, N.A. Krotkov, I. Sprod, and G.J.S. Bluth (1995) Volcanic sulfur dioxide measurements from the total ozone mapping spectrometer instruments. *J. Geophys. Res.*, 100(D7), 14057-14076, 10.1029/95JD01222.

Krueger, A., Krotkov, N. and Yang, K., "Comparison of GOME-2 and OMI sulfur dioxide retrievals", Atmospheric Science Conference Barcelona, Spain, 7-11 September 2009.

Li, C., J. Joiner, N. A. Krotkov, and P. K. Bhartia (2013), A fast and sensitive new satellite SO2 retrieval algorithm based on principal component analysis: Application to the ozone monitoring instrument, Geophys. Res. Lett., 40, 6314–6318, doi:10.1002/2013GL058134.

Puķīte, J., Kühl, S., Deutschmann, T., Platt, U., and Wagner, T.: Extending differential optical absorption spectroscopy for limb measurements in the UV, Atmos. Meas. Tech., 3, 631-653, 2010.

Richter, A., M. Begoin, A. Hilboll, and J. P. Burrows (2011), An improved NO_2 retrieval for the GOME-2 satellite instrument, Atmos. Meas. Tech., 4, 1147–1159, doi:10.5194/amt-4-1147-2011.

Rix, M., Valks, P., Hao, N., Loyola, D. G., Schlager, H., Huntrieser, H. H., Flemming, J., Koehler, U., Schumann, U., and Inness, A.: Volcanic SO_2, BrO and plume height estimations using GOME-2 satellite measurements during the eruption of Eyjafjallajökull in May 2010, J. Geophys. Res., 117, D00U19, doi:10.1029/2011JD016718, 2012.

SACS, Support to Aviation Control Service, SO2 maps available in near-real-time at http://sacs.aeronomie.be.

Spurr, R. J. D., T. P. Kurosu, and K. V. Chance: A Linearized discrete Ordinate Radiative Transfer Model for Atmospheric Remote Sensing Retrieval, J. Quant. Spectrosc. Radiat. Transfer, 68, 689-735, 2001.

Taubman, B. F., J. C. Hains, A. M. Thompson, L. T. Marufu, B. G. Doddridge, J. W. Stehr, C. A. Piety, and R. R. Dickerson (2006), Aircraft vertical profiles of trace gas and aerosol pollution over the mid- Atlantic United States: Statistics and meteorological cluster analysis, J. Geophys. Res., 111, D10S07, doi:10.1029/2005JD006196.

Theys, N., I. De Smedt, J. van Gent, T. Danckaert, T. Wang, F. Hendrick, T. Stavrakou, S. Bauduin, L. Clarisse, C. Li, N. A. Krotkov, H. Yu, M. Van Roozendael, Sulfur dioxide vertical column DOAS retrievals from the Ozone Monitoring Instrument: Global observations and comparison to ground-based and satellite data, J. Geophys. Res. Atmos., 120, doi:10.1002/2014JD022657, 2015.

Walker, J. C., E. Carboni, A. Dudhia, and R. G. Grainger (2012), Improved detection of sulphur dioxide in volcanic plumes using satellite-based hyperspectral infrared measurements: Application to the Eyjafjallajökull 2010 eruption, J. Geophys. Res., 117, D00U16, doi:10.1029/2011JD016810.

Wang, T., Hendrick, F., Wang, P., Tang, G., Clémer, K., Yu, H., Fayt, C., Hermans, C., Gielen, C., Müller, J.-F., Pinardi, G., Theys, N., Brenot, H., and Van Roozendael, M.: Evaluation of tropospheric SO_2 retrieved from MAX-DOAS measurements in Xianghe, China, Atmos. Chem. Phys., 14, 11149-11164, doi:10.5194/acp-14-11149-2014, 2014.

Yang, K., N. Krotkov, A. Krueger, S. Carn, P. K. Bhartia, and P. Levelt (2007), Retrieval of Large Volcanic SO_2 columns from the Aura Ozone Monitoring Instrument (OMI): Comparisons and Limitations, *J. Geophys. Res*., 112, D24S43, doi:10.1029/2007JD008825

E.2.2 Technical notes

Theys et al., 2013, OM3SAF SO2 validation report, TN-IASB-GOME-2B-O3MSAF-SO2-2013.

van Geffen, J., Van Roozendael, M., Rix, M., Valks, P.: Initial validation of GOME-2 GDP 4.2 SO_2 total columns (OTO/SO2) – ORR B, O3MSAF validation report, TN IASB-GOME2-O3MSAF-SO2-01.1, 2008.

Valks et al., 2015 ; Algorithm Theoretical Basis Document for GOME-2 Total Column Products of Ozone, NO2, BrO, HCHO, SO2, H2O and Cloud Properties (GDP 4.8 for O3M-SAF OTO and NTO), DLR/GOME-2/ATBD/01/3/A